PHYSICAL REVIEW D **68**, 035007 (2003)

Detailed study of gluino decay into third generation squarks at the CERN LHC

Junji Hisano
ICRR, University of Tokyo, Kashiwa 277-8582, Japan

Kiyotomo Kawagoe
Department of Physics, Kobe University, Kobe 657-8501, Japan

Mihoko M. Nojiri
YITP, Kyoto University, Kyoto 606-8502, Japan

(Received 7 May 2003; published 14 August 2003)

In supersymmetric models a gluino can decay into $tb\tilde{\chi}_1^{\pm}$ through a top squark (stop) or a sbottom. The decay chain produces an edge structure in the m_{tb} distribution. Monte Carlo simulation studies show that the end point and edge height would be measured at the CERN LHC by using a sideband subtraction technique. The stop and sbottom masses as well as their decay branching ratios are constrained by the measurement. We study interpretations of the measurement in the minimal supergravity model. We also study the gluino decay into $tb\tilde{\chi}_2^{\pm}$ as well as the influence of the stop left-right mixing on the m_{bb} distribution of the tagged tb events.

DOI: 10.1103/PhysRevD.68.035007 PACS number(s): 12.60.Jv, 14.80.Ly

I. INTRODUCTION

The minimal supersymmetric standard model (MSSM) is one of the promising extensions of the standard model [1]. The model requires superpartners of the standard model particles (sparticles), and the Large Hadron Collider (LHC) at CERN might confirm the existence of the new particles [2]. The LHC is a pp collider at $\sqrt{s}=14$ TeV, whose operation is currently expected to start in 2007. The integrated luminosity will be 10 fb^{-1}/yr at the beginning (low-luminosity runs) and then upgraded to 100 fb^{-1}/yr (high-luminosity runs).

Supersymmetry (SUSY) must be broken and the sparticle mass spectrum depends on the SUSY breaking mechanism. Measurement of the sparticle masses provides a way to probe the origin of the SUSY breaking in nature. The sparticle mass measurement at the LHC has been therefore extensively studied.

Among the sparticles the third generation squarks, top squarks (stops) ($\tilde{t}_i$) and sbottoms ($\tilde{b}_i$)($i=1,2$), get special imprints from physics at the very high energy scale. One of the examples is found in a model with universal scaler masses. Although the scalar masses are universal at a high energy scale, the third generation squarks are much lighter than the first and second generation squarks due to the Yukawa running effect. On the other hand, some SUSY breaking models, such as the flavor U(2) model [3] or the decoupling solution [4], and the superconformal model [5] for the SUSY flavor problem, have nonuniversal boundary conditions for the third generation mass parameters at the grand unified theory (GUT) scale. In addition, the $\tilde{t}_L$-$\tilde{t}_R$-Higgs trilinear coupling A_t is comparable to the gluino mass at the weak scale when the origin of the SUSY breaking comes from the GUT scale or Planck scale physics. This appears in the stop mass matrix with a large coefficient m_t: $m_{LR}^2=m_t(A_t-\mu\cot\beta)$. The stop left-right mixing is therefore expected to be sizable, leading to an even lighter stop mass compared to those of other squarks [6]. It should be stressed that the stop masses and mixing are very important parameters to predict the light Higgs boson mass [7] or the rare B decay ratios [8].

We may be able to access the nature of the stop and sbottom at the LHC provided that they are lighter than the gluino ($\tilde{g}$). They may copiously arise from gluino decay if the decay is kinematically allowed. The relevant decay modes for $\tilde{b}_i(i=1,2)$, $\tilde{t}_1$, to charginos $\tilde{\chi}_j^{\pm}$ ($j=1,2$) or neutralinos $\tilde{\chi}_j^0(j=1,2,3,4)$ are listed below[1] (indices to distinguish a particle and its antiparticle is suppressed unless otherwise stated):

$$\begin{aligned}
&(\mathrm{I})_j && \tilde{g}\to b\tilde{b}_1\to bb\tilde{\chi}_j^0 \;\; (\to bbl^+l^-\tilde{\chi}_1^0),\\
&(\mathrm{II})_j && \tilde{g}\to t\tilde{t}_1\to tt\tilde{\chi}_j^0,\\
&(\mathrm{III})_j && \tilde{g}\to t\tilde{t}_1\to tb\tilde{\chi}_j^{\pm},\\
&(\mathrm{III})_{ij} && \tilde{g}\to b\tilde{b}_i\to bW\tilde{t}_1\to bbW\tilde{\chi}_j^{\pm},\\
&(\mathrm{IV})_{ij} && \tilde{g}\to b\tilde{b}_i\to tb\tilde{\chi}_j^{\pm}.
\end{aligned} \tag{1}$$

In previous literature [2,9], the lighter sbottom $\tilde{b}_1$ is often studied through the mode $(\mathrm{I})_2$: namely, the $bb\tilde{\chi}_2^0\to bbl^+l^-\tilde{\chi}_1^0$ channel. This mode is important when the second lightest neutralino $\tilde{\chi}_2^0$ has substantial branching ratios into leptons. The difference of sparticle masses such as $(m_{\tilde{g}}-m_{\tilde{b}_1})$ is determined by measuring kinematical end points of invariant mass distributions for signal events.

In a previous paper [10] we proposed to measure the edge position of the m_{tb} distribution for the modes $(\mathrm{III})_1$ and $(\mathrm{IV})_{11}$, where m_{tb} is the invariant mass of a top-bottom (tb)

---

[1] We do not consider gluino decay into $t\tilde{t}_2$ for this paper.

0556-2821/2003/68(3)/035007(20)/$20.00

system. The decay modes are expected to be dominant in the minimal supergravity (MSUGRA) model, since the branching ratios $\mathrm{Br}(\tilde{b}_1(\tilde{t}_1)\rightarrow t(b)\tilde{\chi}_1^{\pm})$ could be as large as 60%. We focused on the reconstruction of hadronic decays of the top quark, because the m_{tb} distribution of the decay makes a clear "edge" in this case. The parton level m_{tb} distributions for modes $(\mathrm{III})_j$ and $(\mathrm{IV})_{ij}$ are expressed as functions of $m_{\tilde{g}}$, $m_{\tilde{t}_1}$, $m_{\tilde{b}_i}$, and the chargino mass $m_{\tilde{\chi}_j^{\pm}}$: $d\Gamma/dm_{tb}\propto m_{tb}$ and the edge position (end point) of the m_{tb} distribution M_{tb} for the modes $(\mathrm{III})_j$ and $(\mathrm{IV})_{ij}$ are written as follows:

$$M_{tb}^2(\mathrm{III})_j = m_t^2 + \frac{m_{\tilde{t}_1}^2 - m_{\tilde{\chi}_j^{\pm}}^2}{2m_{\tilde{t}_1}^2}\{(m_{\tilde{g}}^2 - m_{\tilde{t}_1}^2 - m_t^2) + \sqrt{[m_{\tilde{g}}^2-(m_{\tilde{t}_1}-m_t)^2][m_{\tilde{g}}^2-(m_{\tilde{t}_1}+m_t)^2]}\},$$

$$M_{tb}^2(\mathrm{IV})_{ij} = m_t^2 + \frac{m_{\tilde{g}}^2 - m_{\tilde{b}_i}^2}{2m_{\tilde{b}_i}^2}\{(m_{\tilde{b}_i}^2 - m_{\tilde{\chi}_j^{\pm}}^2 + m_t^2) + \sqrt{[m_{\tilde{b}_i}^2-(m_{\tilde{\chi}_j^{\pm}}-m_t)^2][m_{\tilde{b}_i}^2-(m_{\tilde{\chi}_j^{\pm}}+m_t)^2]}\}. \tag{2}$$

The measurement of the end points is sensitive to both $m_{\tilde{t}_1}$ and $m_{\tilde{b}_1}$, provided that $m_{\tilde{g}}$ and $m_{\tilde{\chi}^{\pm}}$ are determined from other measurements. The edge height is then closely related to $\sigma(pp\rightarrow\tilde{g}X)\times\mathrm{Br}(\mathrm{III/IV})$. In some model parameters $M_{tb}(\mathrm{III})_1$ is very close to $M_{tb}(\mathrm{IV})_{11}$. When they are experimentally indistinguishable, it is convenient to define a weighted mean of the end points:

$$M_{tb}^{\mathrm{w}} = \frac{\mathrm{Br}(\mathrm{III})M_{tb}(\mathrm{III})_1 + \mathrm{Br}(\mathrm{IV})_{11}M_{tb}(\mathrm{IV})_{11}}{\mathrm{Br}(\mathrm{III})+\mathrm{Br}(\mathrm{IV})_{11}},$$

$$\mathrm{Br}(\mathrm{III}) \equiv \mathrm{Br}(\mathrm{III})_1 + \mathrm{Br}(\mathrm{III})_{11} + \mathrm{Br}(\mathrm{III})_{21}. \tag{3}$$

As the final states bbW from the decay chain $\tilde{g}\rightarrow b\tilde{b}_i \rightarrow bW\tilde{t}_1\rightarrow bbW\tilde{\chi}_1^{\pm}$ [mode $(\mathrm{III})_{i1}$] could have an irreducible contribution to the tb final state, they are included in the definition of M_{tb}^{w}.

In the previous paper we showed that the weighted mean M_{tb}^{w} was successfully measured from a fit to the m_{tb} distribution. We also discussed the interpretation of the measurement. In this paper we significantly extend our study to the branching ratio measurements, identification of the stop and sbottom decays into heavier charginos, and the interpretation in the MSUGRA model.

This paper is organized as follows. In Sec. II, we explain our reconstruction and fitting procedure of the edge structure in detail. We use a sideband method to estimate the background distribution due to misreconstructed events, which plays a key role in the edge reconstruction. Monte Carlo simulations show that the distribution of the signal modes (III) and (IV) after subtracting the sideband background is very close to the parton level distribution. In Sec. III, we explore the MSUGRA parameter space to check if our fitting procedure reproduces the end point M_{tb}^{w} and the number of events going through the decay modes (III) and (IV). We then turn to more delicate issues such as extraction of branching ratios. In Sec. IV, we discuss the stop and sbottom decays into the heavier chargino $\tilde{\chi}_2^{\pm}$ by looking into the m_{tb} distribution of events with additional leptons. In Sec. V, we study the MSUGRA parameter region where the decay modes (III) and/or (IV) are open, and discuss how to extract the fundamental parameters using the m_{tb} distributions. The LHC's potential to extract the top polarization arising from the decay $\tilde{g}\rightarrow t\tilde{t}_1$ is discussed in Sec. VI. Section VII is devoted to conclusions.

TABLE I. Sparticle masses in GeV and the total SUSY cross section (σ_{SUSY}) in pb for the parameter points studied in this paper. The cross sections are calculated by PYTHIA.

	$m_{\tilde{g}}$	$m_{\tilde{t}_1}$	$m_{\tilde{b}_1}$	$m_{\tilde{b}_2}$	$m_{\tilde{\chi}^{\pm}}$	σ_{SUSY}
A1	707	427	570	613	220	26
A2	706	496	587	614	211	25
T1	707	327	570	613	220	30
T2	707	477	570	612	211	25
B	609	402	504	534	179	56
C	931	636	771	805	304	5
G	886	604	714	763	285	7
I	831	571	648	725	265	10
E1	515	273	521	634	153	77
E2	747	524	770	898	232	8

II. SIMULATION AND RECONSTRUCTION

In the MSUGRA model the sparticle spectrum is parametrized by the universal scalar mass m_0, the universal gaugino mass $M_{1/2}$, the trilinear coupling of the scalar fields A_0 at the GUT scale (M_{GUT}), the ratio of the vacuum expectation values $\tan\beta$, and sign of the Higgsino mass parameter μ. In order to demonstrate the end point reconstruction, we take an MSUGRA point with $m_0 = 100$ GeV, $M_{1/2} = 300$ GeV, $A_0 = -300$ GeV, $\tan\beta = 10$, and $\mu > 0$. This corresponds to the sample point A1 in Table I. The masses and mixings of sparticles are calculated by ISASUSY/ISASUGRA 7.51 [11]. Two different event generators, PYTHIA 6.1 [12] and HERWIG 6.4 [13], are utilized to generate Monte Carlo SUSY events using the masses and mixings. In this section we show results with PYTHIA. The events are then passed through a fast detector simulation program for the ATLAS experiment, ATLFAST [14]. This program performs jet reconstruction in the calorimeters and momentum-energy smearing for leptons and photons, giving a list of reconstructed jets as well as identified leptons and photons. We generate a total of 3×10^6 SUSY events, which correspond to an integrated luminosity of 120 fb^{-1}. In addition to the SUSY events, $t\bar{t}$ events are generated using PYTHIA as the standard model background. The number of generated events amounts to 1.94×10^8, corresponding to an integrated luminosity of 286 fb^{-1}. In the plots in this paper, the $t\bar{t}$ background is not included unless otherwise noted.

In the detector simulation, a lepton is identified if $p_T > 5$ GeV and $|\eta| < 2.5$ for an electron and $p_T > 6$ GeV and $|\eta| < 2.5$ for a muon, respectively. A lepton is regarded as isolated if it is separated by $R > 0.4$ from other calorimeter clusters and the transverse calorimeter energy in a cone size $R = 0.2$ around the lepton is less than 10 GeV. The cone size is defined as $R = \sqrt{(\Delta\phi)^2 + (\Delta\eta)^2}$, where ϕ and η are the azimuthal angle and the pseudorapidity, respectively.

By default, jets are reconstructed by a cone-based algorithm with a cone size $R = 0.4$ in the detector simulation.[2] After applying the algorithm, jets having a transverse energy (E_T) more than 10 GeV are kept as reconstructed jets. The b and τ tagging efficiencies are set to be 60% and 50%, respectively. The energy of the reconstructed jet is recalibrated according to its jet flavor using a parametrization optimized to give a proper scale of the dijet mass.

First, we apply the following selection cuts to the simulated events for the tb signal:

(1) The missing transverse energy E_T^{miss} is greater than 200 GeV, where E_T^{miss} is calculated from the reconstructed jets, leptons, photons, and unreconstructed calorimeter energies. This calculation is performed before the recalibration of jet energies.

(2) The effective mass m_{eff} is greater than 1000 GeV, where m_{eff} is the sum of the missing transverse energy and transverse momentum of reconstructed jets: namely, $m_{\mathrm{eff}} = E_T^{\mathrm{miss}} + \Sigma_{all} p_T^{\mathrm{jet}}$.

(3) There are two and only two b jets with $p_T > 30$ GeV in an event.

(4) Excluding the two b jets and those identified as tau jets, the number of remaining reconstructed jets with $p_T > 30$ GeV and $|\eta| < 3.0$ should be between 4 and 6, inclusive.

Distributions of the cut variables are shown in Fig. 1. The first two cuts are to enhance the SUSY events against the standard model background events. The other two cuts are to reduce combinatorial background (wrong combinations of jets) in the reconstruction of the top quark.

To reconstruct the hadronic decay of the top quark, we take the following steps (i)–(iv).

(i) We first take jet pairs consistent with a hadronic W boson decay with a cut on the jet pair invariant mass m_{jj}: $|m_{jj} - m_W| < 15$ GeV. The m_{jj} distribution is shown in Fig. 2(a), where the selected mass region is marked as **W** (the W mass region). Although fake W pairs dominate the distribution, a small bump due to real W bosons can be seen in the mass region.

(ii) The invariant mass of the jet pair and one of the b jets, m_{bjj}, is then calculated. All possible combinations of jet pairs and b jets are tried in an event to select the combination which minimizes the difference $|m_{bjj} - m_t|$. The distribution of the selected m_{bjj} is shown in Fig. 3(a).

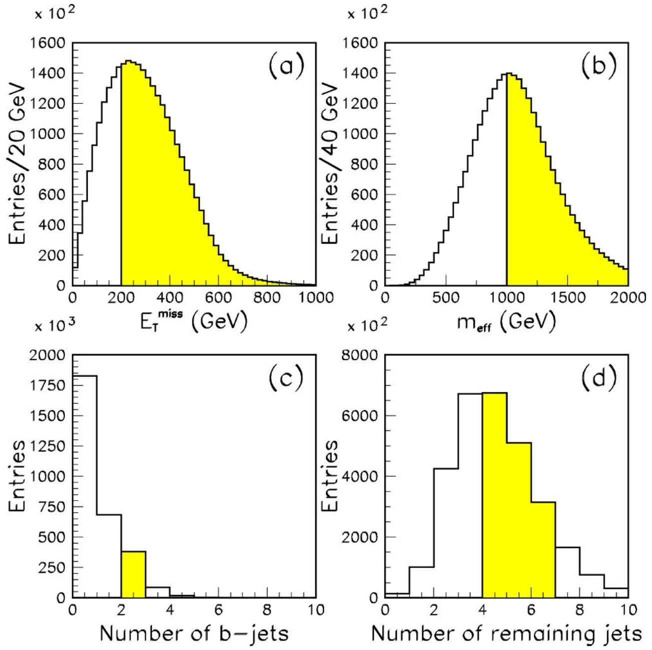

FIG. 1. Distributions of (a) missing transverse energy, (b) effective mass, (c) number of b jets, and (d) number of remaining jets, for 3×10^6 SUSY events at point A1. Accepted regions are hatched.

(iii) The energy and momentum of the jet pair are scaled so that $m_{jj} = m_W$, and the invariant mass m_{bjj} is recalculated. The distribution is shown in Fig. 3(b). The jet combination is regarded as a top quark candidate if $|m_{bjj} - m_t| < 30$ GeV.

As jets are supplied from gluino or squark decays and there are several jets in a selected event, events with a fake W boson (a jet pair that accidentally has $m_{jj} \sim m_W$) still dominate the m_{bjj} distribution. The contribution of the fake W boson in the W mass region is estimated from the events that contain jet pairs with the invariant mass in the regions **A**: $|m_{jj} - (m_W - 30\ \mathrm{GeV})| < 15$ GeV and **B**: $|m_{jj} - (m_W + 30\ \mathrm{GeV})| < 15$ GeV. We call them "the W sidebands." The energy and momentum of the jet pairs are then scaled linearly by multiplying them by a factor $(m_{jj} \pm 30)/m_{jj}$ so

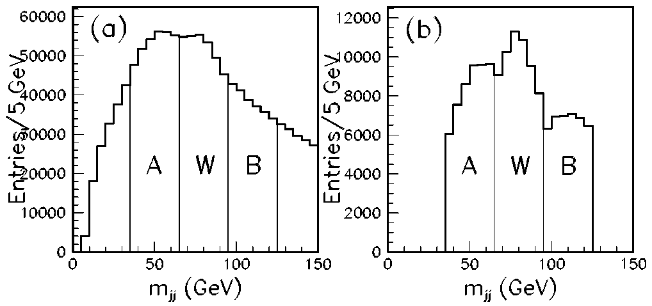

FIG. 2. Distributions of the invariant mass of two jets (a) for all possible combinations and (b) for the combination used to reconstruct a top candidate. **W** and **A**, **B** indicate the W mass region and W sidebands, respectively.

---

[2] Larger R values $R = 0.5$ and 0.6 are also tried to check the dependence on R of the cone-based algorithm. For comparison, another jet reconstruction algorithm, the K_T algorithm, was also tried with $R = 0.4$, 0.5, 0.6, and 0.7. The comparison is given in the Appendix.

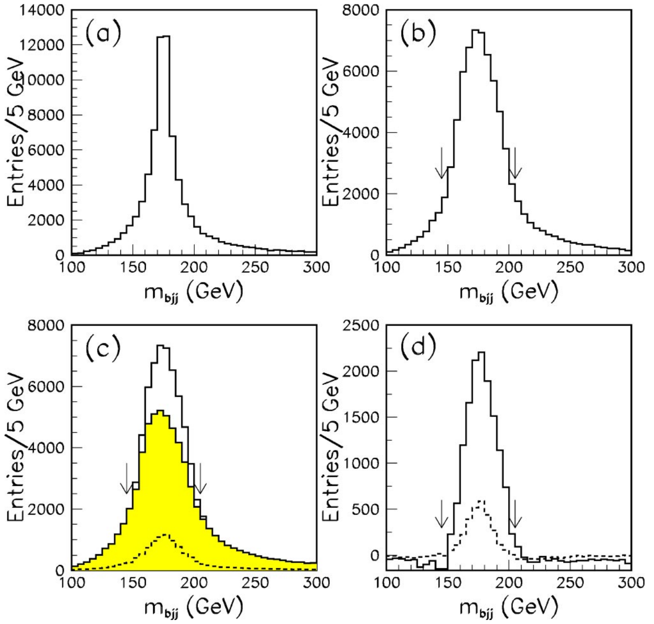

FIG. 3. Distributions of m_{bjj} (a) before and (b) after the jet energy scaling, (c) background estimated by the W sidebands (the hatched histogram) superimposed to the distribution (b), and (d) after subtracting the estimated background. The mass cut for the top candidate is indicated by arrows. Dashed histograms in (c) and (d) show the distributions of $t\bar{t}$ events, where the integrated luminosity of the $t\bar{t}$ events is normalized to that of the SUSY events.

that the jet pairs are in the W mass region $|m_{jj}-m_W| < 15$ GeV. The m_{jj} distributions before the linear scaling are shown for the W region and the W sidebands in Fig. 2(b). The distribution of the fake top quark candidates is estimated by following the same steps (ii) and (iii) for the scaled jet pair [see the hatched histogram in Fig. 3(c)]. The "true" distribution is obtained by subtracting the background distribution estimated by the W sidebands from the original distribution [see Fig. 3(d)]. The estimation is based on an assumption that the background comes from jets without significant correlation with b jets.

The $t\bar{t}$ production is the dominant standard model background. The m_{bjj} distributions of the $t\bar{t}$ events surviving at this stage are shown in Figs. 3(c) and 3(d) before and after sideband background subtraction, respectively. The distribution of the $t\bar{t}$ events is normalized to an integrated luminosity of 120 fb^{-1}, to be compared with that of the SUSY events. To reduce the $t\bar{t}$ events, one of the following two lepton cuts may be used, depending on the signal/background situation.

(a) Loose lepton cut: If there are high-p_T isolated leptons, the invariant mass of any high-p_T lepton and the remaining b jet (m_{bl}) should be greater than 150 GeV. The distribution of the minimum m_{bl} in events with a top candidate is shown in Fig. 4.

(b) Hard lepton cut: An event should have no isolated leptons.

The cuts reduce the fraction of the events having a $t\bar{t}$ pair, where one of the top quarks decays leptonically. The m_{bjj} distributions with the lepton cuts are shown in Fig. 5. The numbers of selected events are listed in Table II. Hereafter we use the loose lepton cut.

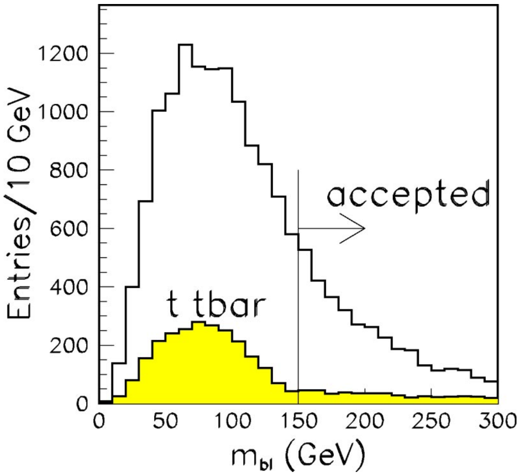

FIG. 4. Distribution of minimum m_{bl} for events having a top candidate. Open and hatched histograms are for SUSY events and $t\bar{t}$ events, respectively. The loose lepton cut is also shown.

For the remaining events, the top candidate is then combined with the other b jet, which is not used to reconstruct the top candidate, to calculate the invariant mass of the tb system m_{tb}. The distribution is shown in Fig. 6(a). However, the expected tb end point is not clearly visible in the m_{tb} distribution due to the fake W events. Here we can again utilize the W sidebands for the background estimation. The estimated background distribution is shown in Fig. 6(b), which is obtained by averaging distributions from the side-

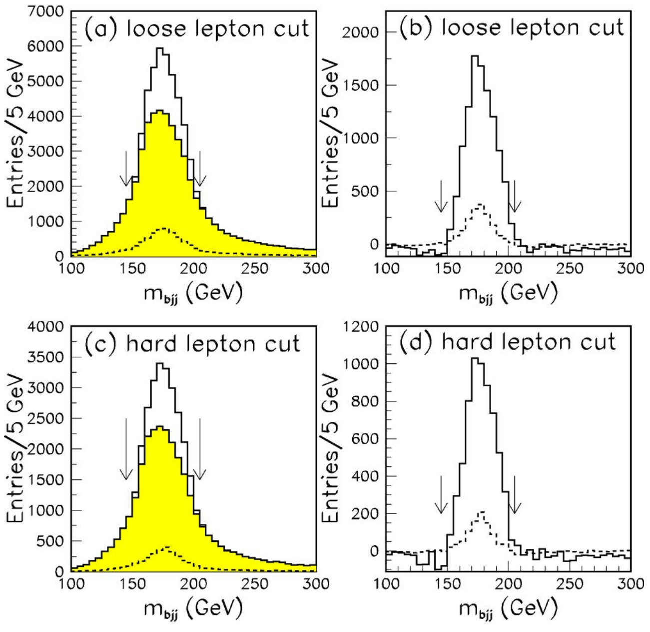

FIG. 5. (a) and (b): Distributions of m_{bjj} with the loose lepton cut before and after sideband subtraction, respectively. (c) and (d): Distributions of m_{bjj} with the hard lepton cut before and after sideband subtraction. The meaning of the histograms is as same as in Figs. 3(c) and 3(d).

TABLE II. Numbers of events having a top candidate with or without lepton cuts. The integrated luminosity is 120 fb^{-1}. The numbers in parentheses are the ratios of the $t\bar{t}$ events to the SUSY events.

	SUSY point A1		$t\bar{t}$	
Sideband subtraction	Before	After	Before	After
No lepton cut	59174	13340	8168 (0.138)	2764 (0.207)
Loose lepton cut	47171	10487	5789 (0.123)	1777 (0.169)
Hard lepton cut	26915	6114	2671 (0.099)	884 (0.145)

bands **A** and **B**. The estimated background distribution is subtracted from the signal distribution in Fig. 6(c). The *corrected* signal distribution (c) shows a better end point structure compared to (a).

By using the information from the event generator, one can show that the sideband method is indeed reproduces the m_{tb} distribution for signal modes (III) and (IV). Figure 6(d) is the same distribution as Fig. 6(c) but for the events which contain either the decay chain $(\mathrm{III})_1$, decay chain $(\mathrm{IV})_{11}$, or decay chains $(\mathrm{III})_{i1}$, which are irreducible to the chain $(\mathrm{III})_1$: $\tilde{g} \to b\tilde{b}_i \to bW\tilde{t}_1 \to bbW\tilde{\chi}_1^{\pm}$. Note that if bW has an invariant mass consistent with a top quark, the decay is kinematically equivalent to mode $(\mathrm{III})_1$. Figure 6(d) shows two end points as expected $[M_{tb}(\mathrm{III})_1 = 471\ \mathrm{GeV}$ and $M_{tb}(\mathrm{IV})_{11} = 420\ \mathrm{GeV}]$, demonstrating that the sideband method works well.

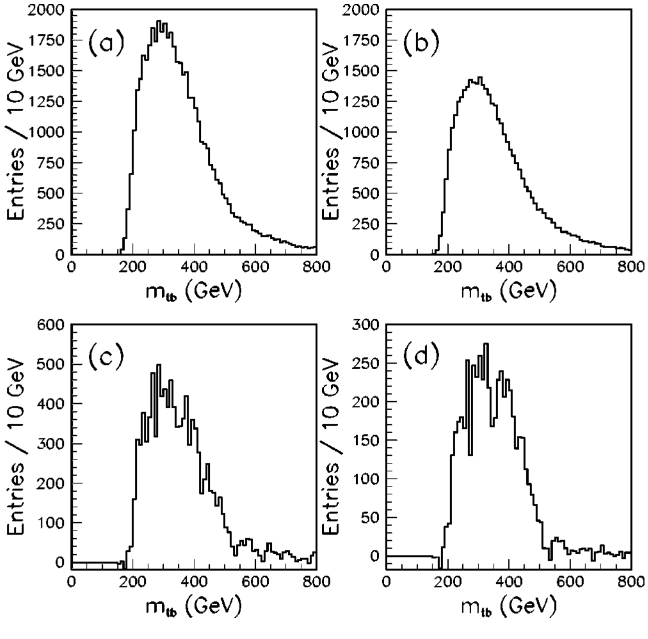

FIG. 6. (a) Signal m_{tb} distribution for the sample point A1 in Table I, (b) the estimated background distribution from the sideband events, (c), (a)–(b), and (d) the m_{tb} distribution for modes $(\mathrm{III})_1$ and $(\mathrm{IV})_{11}$ in Eq. (1), and decay modes $(\mathrm{III})_{i1}$ irreducible to mode $(\mathrm{III})_1$.

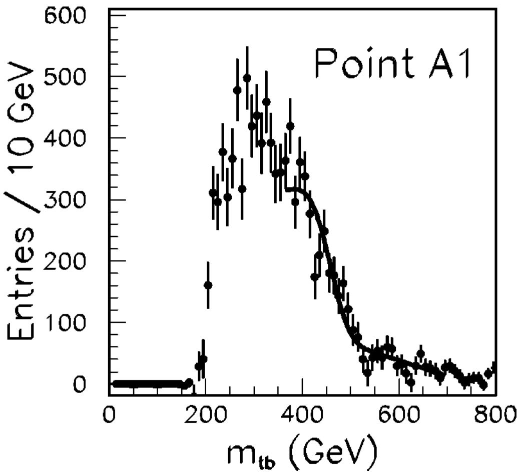

FIG. 7. A fit to the m_{tb} distribution at point A1.

Note that the signals from modes (III) and (IV) in Eq. (1) are significant in the total selected events. The total distribution shown in Fig. 6(c) contains a contribution from misreconstructed events such as other gluino decay chains with W and b jets or stop and sbottom pair productions.

We fit the total distribution shown in Fig. 6(c), which is made with a bin size $\Delta m = 10$ GeV, by a simple fitting function described with the end point M_{tb}^{fit}, edge height h per Δm bin, and smearing parameter σ originated from the jet energy resolution:

$$f(m_{tb}) = \frac{h}{M_{tb}^{\mathrm{fit}}} \int_{m_t}^{M_{tb}^{\mathrm{fit}}} \frac{m}{\sqrt{2\pi}\sigma} \exp\left(-\frac{1}{2}\left[\frac{m - m_{tb}}{\sigma} \right]^2 \right) dm. \tag{4}$$

To reduce the number of free parameters for good convergence capability of the fit, we set the smearing parameter σ to be 10% of the end point M_{tb}^{fit}. This assumption is based on the dijet mass resolution of the ATLAS detector [2]. We assume that the signal distribution is sitting on a linearly decreasing background expressed by a function $a(m_{tb} - M_{tb}^{\mathrm{fit}}) + b$. The parameters a and b are also determined by the fit.

The fit results, especially the edge height h, depend on the mass range used for the fit. We therefore apply an iterative fitting procedure to obtain stable results. The initial M_{tb}^{fit} value is determined by fitting a rather wide mass range $350\ \mathrm{GeV} < m_{tb} < 800\ \mathrm{GeV}$ (45 histogram bins). In the next step, lower 8 bins and higher 25 bins with respect to the M_{tb}^{fit} value are used to obtain new fit results including the new M_{tb}^{fit} value. The relatively small number of lower bins is chosen because the edge height is sensitive to the distribution in the mass region near the end point. Including too many lower bins is found to degrade the sensitivity. The higher bins determines the linearly decreasing background. This step is repeated until the fit results become stable. The number of iterations is typically 3 or 4. If the edge height h has a large fit error, the number of lower bins is increased to 9 or 10, until the error becomes reasonably small (typically less than 15%). The fit result is shown in Fig. 7. We obtain M_{tb}^{fit}

TABLE III. The lighter stop mass and the relevant SUSY mass parameters in GeV and the stop mixing angles for points A1, A2, T1, and T2.

	$m_{\tilde{t}_1}$	$m_{\tilde{t}_R}$	$m_{\tilde{t}_L}$	A_t	$\theta_{\tilde{t}}$
A1	427	482	573	−655	0.99
A2	496	521	591	−457	1.01
T1	327	366	573	−655	1.14
T2	477	551	573	−655	0.84

$=455.2\pm 8.2$ GeV and $h=271\pm 23/(10\text{ GeV})$, where the errors are statistical.

III. M_{tb} DISTRIBUTIONS IN THE SUSY MODEL POINTS

In the previous section we discuss the selection of the *tb* events and the extraction of the edge structure in the m_{tb} distribution originated from the gluino decays $(\mathrm{III})_1$, $(\mathrm{III})_{i1}$, or $(\mathrm{IV})_{i1}$. Two values are obtained from the m_{tb} distribution: the end point M_{tb}^{fit} is directly related to the stop, sbottom, and gluino masses, while the edge height *h* is sensitive to the gluino production cross section and the decay branching ratios.

This section is aimed at comparing the reconstructed values with expectations. We will see that the kinematical quantities M_{tb}^{fit} and the peak value of the effective mass distributions (M_{eff}) agree very well to M_{tb}^{w} and $m_{\tilde{q}}+m_{\tilde{g}}$, respectively. On the other hand, the reconstructed edge height *h*, which is related to the total number of gluinos decaying through the modes (III) or (IV), is dependent on the event generator and also on the decay patterns of the neutralino, chargino, and squarks. We clarify key issues to reduce the uncertainties in this section.

A. Model parameters

The gluino decay widths and decay kinematics depend on the squark masses and mixings. The charginos and neutralinos in the decay chains (I)–(IV) further decay into jets and leptons, and the decay patterns depend on the electroweak SUSY parameters such as μ, M_1, M_2, $\tan\beta$, and the slepton masses. The m_{tb} distribution is therefore a function of all SUSY parameters. To check the validity of our reconstruction and subtraction scheme, we study the m_{tb} distributions for various sets of SUSY parameters.

The reference point A1 introduced in the previous section corresponds to the MSUGRA model with a large negative A_0 value. The stop and sbottom masses can be changed by varying the A_0 value without changing other sparticle masses drastically (see Sec. V for details). We thus make another MSUGRA point A2, by changing only the A_0 value from −300 GeV to 300 GeV from point A1. In addition, two non-MSUGRA points T1 and T2 are made from point A1, where the chargino-neutralino sector and the gluino mass are kept unchanged but the stop masses and mixing are modified by changing the mass parameter $m_{\tilde{t}_R}$. The stop mass parameters and the mixing angle at the low-energy scale are listed in Table III.

TABLE IV. The universal parameters at the GUT scale for the points we study. Units are in GeV except $\tan\beta$.

	$M_{1/2}$	$m_0(\tilde{q})$	$m_0(H)$	A_0	$\tan\beta$
A1	300	100	100	−300	10
A2	300	100	100	300	10
B	255	102	102	0	10
C	408	92	92	0	10
G	383	125	125	0	20
I	358	188	188	0	35
E1	200	500	200	−1000	10
E1	300	700	500	−1000	10

Next we choose MSUGRA points B, C, G, and I, which were discussed in Ref. [15]. They satisfy $m_{\tilde{g}}>m_{\tilde{t}_1}+m_t$ so that the decay mode $(\mathrm{III})_1$ is open. The points also satisfy the condition $m_{\tilde{g}}<1$ TeV, which is required for a statistical reason. The gluino production is dominated by the process $qg\to\tilde{q}\tilde{g}$ in the case of $m_{\tilde{q}}\sim m_{\tilde{g}}$, and the production cross section is parametrized as [16]

$$\sigma(\tilde{q}\tilde{g})+\sigma(\tilde{q}^*\tilde{g})=1.74\times\left(\frac{m_{\tilde{g}}}{\mathrm{TeV}}\right)^{-5.78}(\mathrm{pb}). \qquad (5)$$

For example, the cross section is 14 pb and 3.1 pb for $m_{\tilde{g}}=700$ GeV and 900 GeV, respectively. Assuming that the branching ratios and reconstruction efficiency are equal to those of point A1, the gluino mass must be less than 1 TeV to reconstruct more than 2000 SUSY *tb* events after sideband subtraction for an integrated luminosity of 100 fb^{-1}.

Finally we select two more points E1 and E2, where only the decay chain $(\mathrm{III})_1$ is kinematically open and the other two-body gluino decays into squarks are closed. This happens when m_0 and A_0 are large. As the SUSY events at these points typically contain four bottom quarks, the combinatorial background for the *tb* reconstruction is significantly large.

For the points we study in this paper, we list the relevant sparticle masses and the universal parameters at the GUT scale in Tables I and IV, respectively. At each SUSY point we generate two Monte Carlo data samples, each having 3×10^6 events, where one is generated by PYTHIA and the other by HERWIG. The cross sections are summarized in Table I. The cross section is largest for point E1, where the generated 3×10^6 events correspond to 39 fb^{-1}. The SUSY cross section for point C is the smallest among them, where the generated 3×10^6 events correspond to an integrated luminosity of 600 fb^{-1}. Note we use the *b* tagging efficiency for low-luminosity run $\epsilon_b=0.6$ throughout our simulation. However for the high-luminosity run $\epsilon_b=0.5$ should be used. The number of reconstructed events should be scaled by 0.7 $(\sim(0.5/0.6)^2)$ in addition to the scaling due to the luminosity for points C, G, I, and E1, because the cross sections are small for these points.

TABLE V. Fit results of the m_{tb} distributions and numbers of tb events after the sideband subtraction N_{edge} and N_{all} for 3×10^6 Monte Carlo events. M_{tb}^{w} and M_{tb}^{fit} are given in GeV. The fit does not include the $t\bar{t}$ background, and the loose lepton cut is applied. N_{all} is the total number of tb events, while N_{edge} is the number of events with one and only one gluino decays into mode $(\mathrm{III})_1$, $(\mathrm{III})_{i1}$, or $(\mathrm{IV})_{i1}$. "PY" is for PYTHIA and "HW" is for HERWIG. The number of degrees of freedom of the fit is between 30 and 32.

	Gen	M_{tb}^{w}	M_{tb}^{fit}	$h/(10\mathrm{GeV})$	χ^2	N_{edge}	N_{all}
A1	PY	459	455.2 ± 8.3	271.4 ± 22.7	41.3	5846	10487
	HW		434.5 ± 5.8	354.8 ± 23.3	36.9	6685	11470
A2	PY	409	442.0 ± 17.5	153.0 ± 20.6	45.2	3064	7525
	HW		394.4 ± 9.5	190.6 ± 21.8	23.5	3095	7805
T1	PY	468	460.3 ± 5.4	327.0 ± 21.6	25.5	6620	11659
	HW		452.0 ± 3.9	447.5 ± 23.5	46.0	8170	14050
T2	PY	429	434.5 ± 8.1	223.2 ± 21.6	27.0	4461	8466
	HW		416.6 ± 5.2	321.0 ± 23.2	28.5	5378	9592
B	PY	371	385.6 ± 6.3	226.9 ± 19.6	42.7	2801	5396
	HW		361.7 ± 7.3	223.5 ± 21.3	42.4	3105	5935
C	PY	557	548.2 ± 14.1	142.4 ± 17.5	30.6	4026	11228
	HW		556.3 ± 9.4	178.2 ± 17.9	30.5	4395	12704
G	PY	533	498.5 ± 8.6	244.1 ± 23.8	35.2	5784	13630
	HW		506.9 ± 6.4	325.5 ± 22.9	33.6	6248	15039
I	PY	507	497.8 ± 7.3	289.7 ± 24.0	28.4	6016	13752
	HW		492.9 ± 5.2	383.9 ± 24.5	31.9	6661	14968
E1	PY	360	345.5 ± 5.3	270.6 ± 23.7	19.1	2778	4595
	HW		348.0 ± 6.3	251.5 ± 23.9	25.1	3169	5167
E2	PY	453	430.8 ± 7.5	352.0 ± 33.9	34.6	5577	16490
	HW		444.7 ± 8.0	324.6 ± 30.9	45.5	4394	15724

TABLE VI. Branching ratios of gluino cascade decays in percent. Decay modes (III) and (IV) are defined in Eq. (1). The "sum" is the total of all $(\mathrm{III})_1$, $(\mathrm{III})_{i1}$, and $(\mathrm{IV})_{i1}$ decay modes. The "bbX" is the branching ratio of the gluino decaying into $\tilde{t}_i$ or $\tilde{b}_i$, so that two bottom quarks appear in the decay products.

	$(\mathrm{III})_1$	$(\mathrm{IV})_{11}$	$(\mathrm{IV})_{21}$	$(\mathrm{III})_{11}$	$(\mathrm{III})_{21}$	Sum	bbX
A1	11.0	6.7	1.4	3.4	2.7	25.3	43.4
A2	3.1	6.5	1.6	1.4	0.4	13.1	32.0
T1	24.5	3.2	0.8	5.0	3.0	36.5	56.3
T2	4.3	9.9	2.2	0.5	2.1	19.0	36.2
B	4.1	8.2	2.3	0.9	1.7	17.3	33.5
C	7.2	5.3	1.3	0.9	0.8	15.4	38.5
G	6.6	7.5	1.2	0.5	0.8	16.6	40.4
I	6.2	11.1	0.7	0.0	0.7	18.7	47.3
E1	78.5	0	0	0	0	78.5	99
E2	42.6	0	0	0	0	42.6	98

B. Reconstruction of kinematic variables

The fit results of the m_{tb} distributions are listed in Table V, where we follow the fitting procedure described in the previous section. The weighted end point M_{tb}^{w} is defined in Eq. (3) and the relevant branching ratios are listed in Table VI. In Table V, N_{all} is the number of tb events after the sideband subtraction, while N_{edge} is the number of tb events after the subtraction, with one and only one gluino decaying through mode $(\mathrm{III})_1$, $(\mathrm{III})_{i1}$, or $(\mathrm{IV})_{i1}$. Generator information is used to obtain N_{edge}.

The relation between M_{tb}^{fit} and M_{tb}^{w} is shown in Fig. 8. The fitted value M_{tb}^{fit} increases linearly with the weighted end point M_{tb}^{w} in the mass range 350 GeV$<M_{tb}^{\mathrm{w}}<$600 GeV and tends to be lower than M_{tb}^{w}. In the previous literature [2,9], the lower mass value was understood as the effect of particles missed outside the jet cones. In the literature invariant mass distributions of the events with same flavor and opposite sign leptons are studied, which come from the cascade decay of the squarks $\tilde{q}\to q\tilde{\chi}_2^0\to ql\tilde{l}\to qll\tilde{\chi}_1^0$. The end point of the m_{jll} distribution is lower than the parton level qll end point by about 10%.

In the study of the squark cascade decay $\tilde{q}\to qll\tilde{\chi}_1^0$, the end point agrees better with the parton level one by changing the jet cone size to $R=0.7$. In our study at the reference point A1, the reconstructed number of events is significantly reduced for $R=0.7$. We find that using a jet cone size $R=0.5$ leads to a better reconstruction and a larger M_{tb}^{fit}, which is closer to M_{tb}^{w}. Such a comparison might be useful to estimate the true end point. We discuss the dependence on the jet finding algorithm and the cone parameters in the Appendix.

We note that our definition of M_{tb}^{w} might be too simple if the reconstruction efficiencies of decay modes (III) and (IV) are very different. In addition, the weighted average should not be applied when $M_{tb}(\mathrm{III})_1$ and $M_{tb}(\mathrm{IV})_{11}$ differ by more

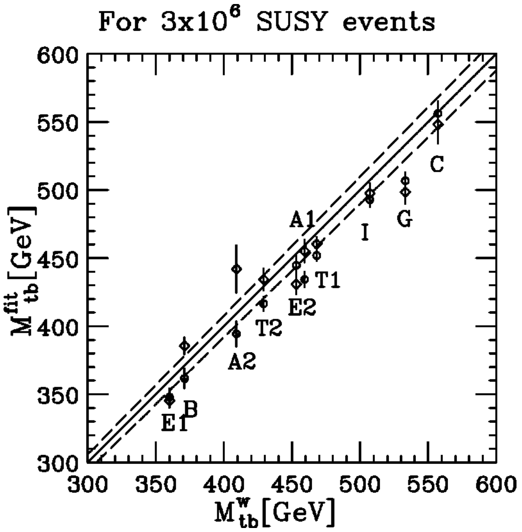

FIG. 8. Relation between M_{tb}^{w} and M_{tb}^{fit} for the sample points. The solid line corresponds to $M_{tb}^{\mathrm{w}}=M_{tb}^{\mathrm{fit}}$ and dashed lines to $M_{tb}^{\mathrm{w}}(1\pm0.02)=M_{tb}^{\mathrm{fit}}$. Bars with a diamond and a circle correspond to PYTHIA and HERWIG samples, respectively.

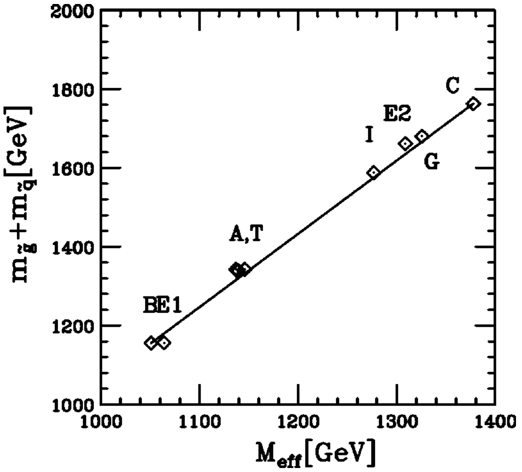

FIG. 9. Relation between $M_{\rm eff}$ and $m_{\tilde g}+m_{\tilde q}$ for the sample points in Table I (HERWIG samples). The line shows a linear fit of $m_{\tilde g}+m_{\tilde q}$ as a function of $M_{\rm eff}$.

than 80 GeV, as we use events with $m_{tb}>M_{tb}^{\rm fit}-80$ GeV for the fit.

We now discuss the relation between $M_{\rm eff}$ and $m_{\tilde g}, m_{\tilde q}$ using the *tb* samples. We find that the sum of the masses $m_{\tilde g}+m_{\tilde q}$ has a linear dependence on $M_{\rm eff}$ as shown in Fig. 9. The deviation of the sample points from a linear fit is less than 5%. The plot is for HERWIG samples, and we find that PYTHIA and HERWIG give consistent results for the relation between $M_{\rm eff}$ and the masses.

The *tb* sample contains two and only two *b* jets originating from a gluino decay; therefore, the $m_{\tilde g}$ dependence of $M_{\rm eff}$ is expected. One may wonder that the $\tilde g\tilde g$ production might affect the $M_{\rm eff}$ value. This is, however, not the case for the points we study. Indeed, points E1 and E2, where $m_{\tilde q} \gg m_{\tilde g}$, also satisfy the linear relation between $M_{\rm eff}$ and $m_{\tilde q}+m_{\tilde g}$. Note that the quark parton distribution is harder than the gluon parton distribution. Therefore $\sigma(pp\to\tilde q\tilde g) \gg \sigma(pp\to\tilde g\tilde g)$ in a wide MSSM parameter region. This is why $M_{\rm eff}$ becomes a very good function of $m_{\tilde g}+m_{\tilde q}$.

In Ref. [17] the relation between $M_{\rm eff}$ and the effective SUSY scale is studied, where the effective SUSY scale is defined as the cross-section-weighted mean of the masses of two sparticles initially produced in *pp* collisions. On the other hand, we actively select the $\tilde g\tilde q$ productions by requiring two tagged *b* jets. This leads to a clear dependence of $M_{\rm eff}$ and $m_{\tilde q}+m_{\tilde g}$.

C. Number of *tb* events

We now discuss the relation between the edge height *h*, the number of reconstructed *tb* events, and the reconstruction efficiencies. The total number of the "edge" events, $N_{\rm edge}$, arising from decay chains (III) and (IV) may be estimated from $M_{tb}^{\rm fit}$, *h* per bin size Δm, as follows:

$$N_{\rm edge}\sim N_{\rm fit}=\frac{h}{2}\left(\frac{m_t}{M_{tb}^{\rm fit}}+1\right)\frac{M_{tb}^{\rm fit}-m_t}{\Delta m}. \tag{6}$$

This formula is obtained by assuming the parton level distribution. The factor $m_t/M_{tb}^{\rm fit}+1$ comes from the fact that $m_{tb} \geq m_t$ for the signal distribution and equating the minimum of the m_{tb} distribution from decay chain (III) or (IV) to m_t. This is a good approximation for reasonable SUSY parameters.

In Figs. 10(a) and 10(b) we compare $N_{\rm edge}$ in Table V with $N_{\rm fit}$. We find a very good agreement between them for both the PYTHIA and HERWIG samples. On the other hand, the correlation between $N_{\rm all}$ and $N_{\rm fit}$ is much worse as shown in Fig. 10(c). The number $N_{\rm all}$ receives a contribution from other gluino cascade decay chains such as modes (I) and (II), as well as contributions from the stop and sbottom pair productions. By the end point fit, we extract the number of events coming only from modes $({\rm III})_1$, $({\rm III})_{i1}$, and $({\rm IV})_{i1}$.

$N_{\rm edge}$ and, then, $N_{\rm fit}$ must be related to the number of gluino decays through cascade decay chains (III) and (IV) via the reconstruction efficiencies. For the points we study, the number of produced $\tilde g\tilde g$ events, $N(\tilde g\tilde g)$, is typically 10%–14% of the total SUSY production events, while the number of $\tilde q^*\tilde g$ and $\tilde q\tilde g$ production events, $N(\tilde q^*\tilde g)+N(\tilde q\tilde g)$, ranges from 42% to 51%. The gluino decay branchings ratios are listed in Table VI. The number of events, $N_{\rm prod}$, where one gluino decays through modes (III) or (IV) and the other squark or gluino decay does not produce any bottom quark, is given as follows:

$$\begin{aligned} mN_{\rm prod}&=2N(\tilde g\tilde g)[1-{\rm Br}(\tilde g\to bbX)]{\rm Br}({\rm edge})+[N(\tilde g\tilde q)\\ &\quad+N(\tilde g\tilde q^*)]{\rm Br}({\rm edge}),\\ {\rm Br}({\rm edge})&\equiv{\rm Br}({\rm III})_1+{\rm Br}({\rm III})_{11}+{\rm Br}({\rm III})_{21}+{\rm Br}({\rm IV})_{11}, \end{aligned} \tag{7}$$

where ${\rm Br}(\tilde g\to bbX)$ is the branching ratio of the gluino decaying into a stop or sbottom, thus having two bottom quarks in the final state. The reconstruction efficiency of the *tb* edge mode, ϵ_{tb}, is given as

$$\epsilon_{tb}=N_{\rm edge}/N_{\rm prod}. \tag{8}$$

If the efficiency does not strongly depend on the uncertainty in hadronization and the model parameter dependence can be corrected from other measurements, we can extract the number $N_{\rm prod}$ from the experimental data.

The major uncertainty in hadronization may be estimated by the generator dependence of the reconstruction efficiency ϵ_{tb}. The edge height *h* for the HERWIG sample is significantly larger than that of the PYTHIA sample in Table V, except points E1 and E2, and the difference is more than 20% at many points. We note that the difference is small before we apply the sideband subtraction. For example, the numbers of *tb* events before and after sideband subtraction are 9695 (10180) and 2462 (2949) for the PYTHIA (HERWIG) sample, respectively, at point A1. The number of events before sideband subtraction only differs by 5% between HERWIG and PYTHIA, while the difference increases to more than 20% after the subtraction. This indicates that the resolution of the *W* boson mass is somewhat better for the HERWIG sample. Indeed, the major difference of the two generators is in the

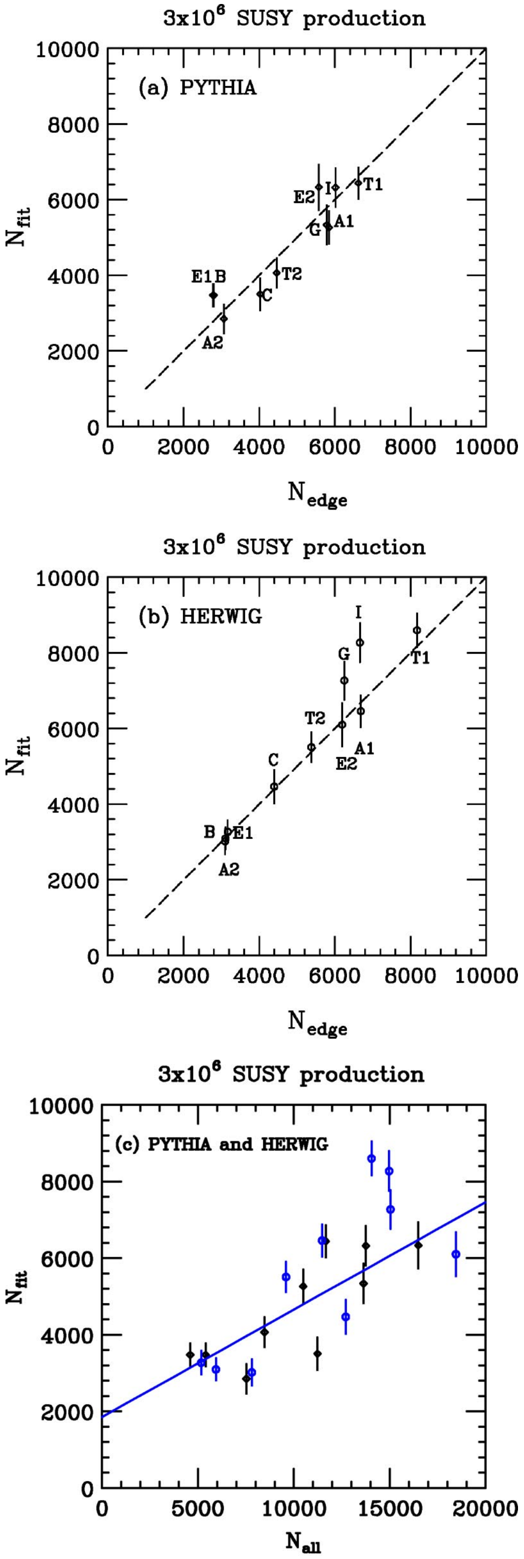

FIG. 10. Relations between $N_{\rm edge}$ and $N_{\rm fit}$ for (a) PYTHIA and (b) HERWIG. (c) Relation between $N_{\rm all}$ and $N_{\rm fit}$. The line in (a) and (b) shows $N_{\rm fit}=N_{\rm edge}$, while the line in (c) is a result of a linear fit.

fragmentation scheme. PYTHIA is based on the string model, while HERWIG is based on the QCD model. Currently we are only able to say that understanding the nature of fragmentation is essential for an interpretation of $N_{\rm fit}$. We compare the HERWIG and PYTHIA samples in the Appendix.

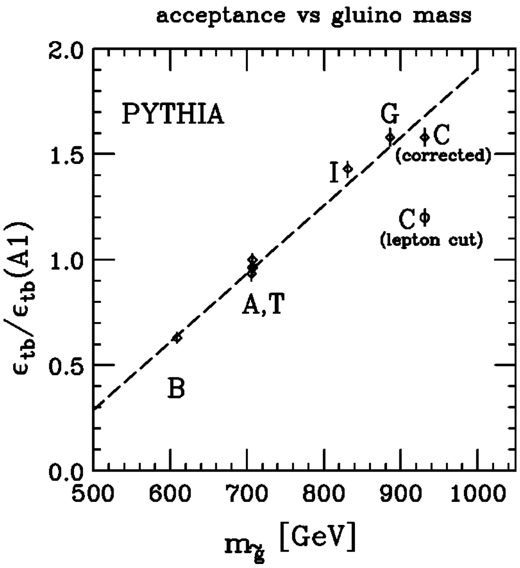

FIG. 11. Reconstruction efficiencies of the model points in Table I relative to that of point A1 as a function of $m_{\tilde g}$. Point C is plotted twice with and without the loose lepton cut.

Let us discuss other effects that might change the reconstruction efficiency. In Fig. 11 we plot the reconstruction efficiency ϵ_{tb} as a function of $m_{\tilde g}$ by normalizing the efficiency to that for point A1. Here $N_{\rm prod}$ is calculated using Eq. (7), the generator information on $N(\tilde g\tilde g)$, $N(\tilde q^{(*)}\tilde g)$, and the Monte Carlo inputs of the gluino branching ratios. The length of the bar in the plot shows twice the statistical error of $N_{\rm edge}$, $\delta(\epsilon_{tb}/\epsilon_{tb}(\mathrm{A1}))=2[\epsilon_{tb}/\epsilon_{tb}(\mathrm{A1})]/\sqrt{N_{\rm edge}}$. We do not discuss points E1 and E2 here because events with two bottom quarks are not the dominant signature of squark and gluino production at these points.

The efficiencies are very close to one another among points A1, A2, T1, and T1. Although the stop mass is very different among the points, the mass has little influence on the efficiency. Note that these points have the same gluino masses and almost the same parameters for the chargino and neutralino sectors. For the other points, the efficiency can also be expressed as a linear function of $m_{\tilde g}$ except the sample point C. The gluino mass dependence arises from the preselection cut $m_{\rm eff}>1000$ GeV.

The reconstruction efficiency at point C (the circle in Fig. 11) is lower by 20% from the linear fit (the dashed line in Fig. 11). This is due to the loose lepton cut which reduces the $t\bar t$ background. As the chargino decay branching ratio into leptons is high (about 47%) at point C, the lepton cut destroys a significant fraction of tb events. The effect is estimated by comparing $N_{\rm edge}$ without any lepton cut and $N_{\rm edge}$ with the loose lepton cut, at points C and A1. The efficiency at point C without any lepton cut is plotted in Fig. 11 and is close to the linear fit of the other points.

The gluino mass dependence of the reconstruction efficiency would be easily corrected by estimating the gluino mass from the effective mass distribution. The uncertainty from the chargino decay branching ratio may be corrected by studying tb final states with leptons as well. Therefore the parameter dependence of the efficiency may be corrected by analyzing the Monte Carlo and real data. Efforts to determine the MSSM parameters are of course very important to this purpose.

D. Branching ratios

In the previous subsection, we found that the reconstruction efficiencies significantly differ between the PYTHIA and HERWIG samples. However, as we can see in Table V, the generator dependence mostly cancels in the ratio $N_{\mathrm{fit}}/N_{\mathrm{all}}$. Therefore the ratio may play a role in determining the fundamental parameters. For example, when the contributions from the stop or sbottom pair productions are negligible, $N_{\mathrm{fit}}/N_{\mathrm{all}}$ is determined by the branching ratios to the third generation squarks. However, there are several aspects one must consider.

N_{all} consists of contributions from various decay modes, even if the contributions from the stop or sbottom pair productions are negligible.

(a) The $t\bar{t}$ final state from the decay chains (II) contributes to N_{all}. The branching ratio is typically 1/3 of that of the tb final state for $\mu > M_2 > M_1$. The $t\bar{t}$ final state is reconstructed as tb with a high probability, although the m_{tb} distribution does not have an edge structure.

(b) We expect that events having no $t \to bW$ decay would be eliminated by the sideband subtraction and should not contribute to N_{all}. However, some events actually remain, because of W and Z^0 bosons from the decay of charginos and neutralinos, as well as accidental W and Z^0 bosons from other cascade decay chains. An example where $\tilde{\chi}_2^0$ decays dominantly into the Z^0 boson will be discussed in the next subsection.

(c) In addition, the sideband subtraction is not necessarily perfect, as will be discussed in the Appendix. For example, the efficiency of mode $(\mathrm{I})_2$ is roughly a half of that of mode $(\mathrm{III})_1$ after sideband subtraction at point A1 (see the Appendix).

(d) The cuts to reduce background events may induce a decay mode dependence of the efficiency. For example, the lepton cut could efficiently reduce the edge mode (III) if $\mathrm{Br}(\tilde{\chi}_1^{\pm} \to lX)$ is large as we have seen in Fig. 11 for point C.

The interpretation of the ratio $N_{\mathrm{fit}}/N_{\mathrm{all}}$ becomes more complicated for the following two cases:

(a) If $m_{\tilde{t}(\tilde{b})} < m_{\tilde{g}} < m_{\tilde{q}}$, squarks mostly decay into the gluino. As discussed previously, the squark-gluino production and decay typically produce events with four b jets. They are identified as a two-b-jet event when two b jets are tagged and the other two are mistagged. These events decrease the fraction from decay chains (III) and (IV) in two-b-jet events. Assuming a tagging efficiency of 60% for a single b jet, 35% of the four bottom quark events are identified as two-b-jet events, and only 1/3 of them contain a b-jet pair originated from a single gluino decay. The wrong b-jet pair combinations significantly dilute the edge mode. Study of events with three b jets and four b jets is necessary for this case.

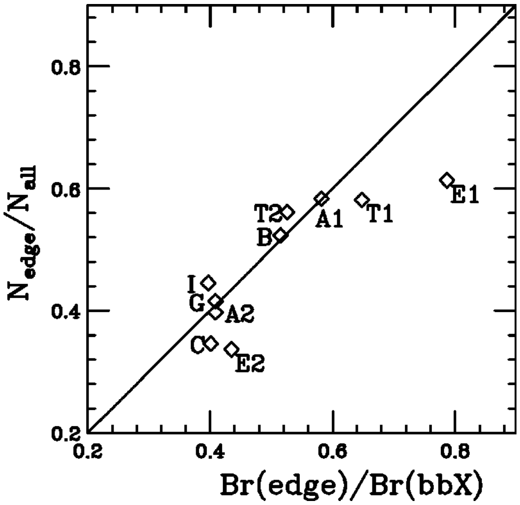

FIG. 12. Relation between $N_{\mathrm{edge}}/N_{\mathrm{all}}$ and $\mathrm{Br(edge)}/\mathrm{Br}(\tilde{g} \to bbX)$.

(b) The tb signal from the stop pair production could be significant if the stop is much lighter than the gluino. For example, only 4.7% of the SUSY events comes from the stop pair production at point A1, while it amounts to be about 17% at point T1.

In the MSUGRA model, both the right-handed stop and left-handed sbottom are lighter than the gluino in a broad parameter space. As a result, decay modes which involve W bosons [modes (II), (III), and (IV)] dominate over gluino decays to bbX in the region. Because events with W bosons remain after W sideband subtraction, the reconstruction efficiency ϵ_{tb} is expected to be similar for those decay modes. Thus, if the contributions from the stop or sbottom pair productions are negligible, the numbers of events with two bottom quarks are given approximately as

$$\begin{aligned} N_{\mathrm{fit}} &\sim \epsilon_{tb}\mathrm{Br(edge)}\{2N(\tilde{g}\tilde{g})[1-\mathrm{Br}(\tilde{g}\to bbX)]+N(\tilde{g}\tilde{q}) \\ &\quad +N(\tilde{g}\tilde{q}^*)\}, \\ N_{\mathrm{all}} &\sim \epsilon_{tb}\mathrm{Br}(\tilde{g}\to bbX)\{2N(\tilde{g}\tilde{g})[1-\mathrm{Br}(\tilde{g}\to bbX)] \\ &\quad +N(\tilde{g}\tilde{q})+N(\tilde{g}\tilde{q}^*)\}. \end{aligned} \tag{9}$$

If this simple formula holds, the ratio $N_{\mathrm{fit}}/N_{\mathrm{all}}$ should provide the ratio of the branching ratios $\mathrm{Br(edge)}/\mathrm{Br}(\tilde{g} \to bbX)$.

This is illustrated in Fig. 12, where we plot the ratio $N_{\mathrm{edge}}/N_{\mathrm{all}}$ as a function of $\mathrm{Br(edge)}/\mathrm{Br}(\tilde{g} \to bbX)$. Here we plot $N_{\mathrm{edge}}/N_{\mathrm{all}}$ instead of $N_{\mathrm{fit}}/N_{\mathrm{all}}$, because we have already seen $N_{\mathrm{fit}} \sim N_{\mathrm{edge}}$, and the statistical fluctuation of N_{edge} is small ($\sim 2\%$) with the help of the generator information. Some points in the plots are away from the line $N_{\mathrm{edge}}/N_{\mathrm{all}} = \mathrm{Br(edge)}/\mathrm{Br}(\tilde{g} \to bbX)$: Point C is off because the

TABLE VII. Fit results for the Snowmass points. Data sample at SPS 2 corresponds to 2×10^6 events, while other samples correspond to 3×10^6 events.

	$M_{tb}^{\rm w}$[GeV]	$M_{tb}^{\rm fit}$[GeV]	$h/(10$ GeV)
SPS 1	380.8	363.9±4.8	267.3±20.8
SPS 2	N/A	484.9±24.9	92.2±23.5
SPS 4	431.0	495.0±6.2	515.7±33.0
SPS 5	416.2	442.6±42.8	56.6±69.6
SPS 6	442.3	416.2±6.2	326.4±24.7

chargino has large branching ratios into leptons as discussed earlier. At point T1, $\tilde t_1 \tilde t_1^*$ production contributes to $N_{\rm all}$. Points E1 and E2 are significantly off because the first and second generation squarks dominantly decay into the gluino.

The systematics due to the chargino and neutralino decay patterns are difficult to estimate from the LHC data only. By combining the data from a future e^+e^- linear collider (LC) of $\sqrt{s}=500$–1000 GeV such systematics would be significantly reduced. Note that SUSY points with $m_{\tilde\chi_1^+} \lesssim 300$ GeV are studied in this paper, which is within the reach of a TeV scale LC.

If events with four b jets dominate the SUSY events at the LHC, study of the events with four or three b jets would be important, which is out of the scope of this paper. If $m_{\tilde t_1} \ll m_{\tilde g}$, it is important to constrain the stop mass in order to estimate the contribution from $\tilde t_1 \tilde t_1^*$, as the cross section increases rapidly as $m_{\tilde t_1}$ decreases. The weighted end point $M_{tb}^{\rm w}$ would provide information on $m_{\tilde t_1}$.

E. Snowmass points

In this subsection we check if we would reconstruct fake end points by any chance when the mode of our interest is insignificant. To this purpose, we generate a set of Monte Carlo data for the Snowmass points [18]. The Snowmass points and slopes (SPS) are a set of benchmark points and parameter lines in the MSSM parameter space corresponding to different scenarios in the search for SUSY at the present and future experiments. Some of those points correspond to the case where decay modes (III) and (IV) are not dominant, and we should not expect to see the edge structure in the m_{tb} distribution.

We list the fit results at SPS 1-2 and 4-6 in Table VII. Here SPS 3 is not listed as it is the same as point C.

The $M_{tb}^{\rm fit}$ is lower by 20 GeV than the $M_{tb}^{\rm w}$ at SPS 1 and SPS 6, similar to the points discussed in Sec. III B (see Table V).

SPS 2 is the so-called "focus point," where the scalar mass at the GUT scale m_0 is larger than the GUT scale gaugino mass $M_{1/2}$. The gluino two-body decays into a squark and a quark are not kinematically open; therefore, the dominant decay modes of the gluino are three-body decays: Br($\tilde g \to tb\tilde\chi_2^\pm$)=25%, Br($\tilde g \to tb\tilde\chi_1^\pm$)=20%, and Br($\tilde g \to tt\tilde\chi_i^{0\prime}s$)=20%. The m_{tb} distribution should not have any edge structure because it dominantly consists of gluino three-body decays. The reconstructed edge has only 4σ in height and is statistically insignificant. The χ^2 value of the fit is also rather large, $\chi^2=44.7$ for 30 degrees of freedom.[3] The fitted end point $M_{tb}^{\rm w}=484.9\pm24.9$ GeV may be related to the mass difference between the gluino and heavier chargino, $m_{\tilde g}=778.6$ GeV and $m_{\tilde\chi_2^\pm}=296.3$ GeV. The m_{tb} distribution at SPS 2 is compared with that at SPS 1 in Fig. 13.

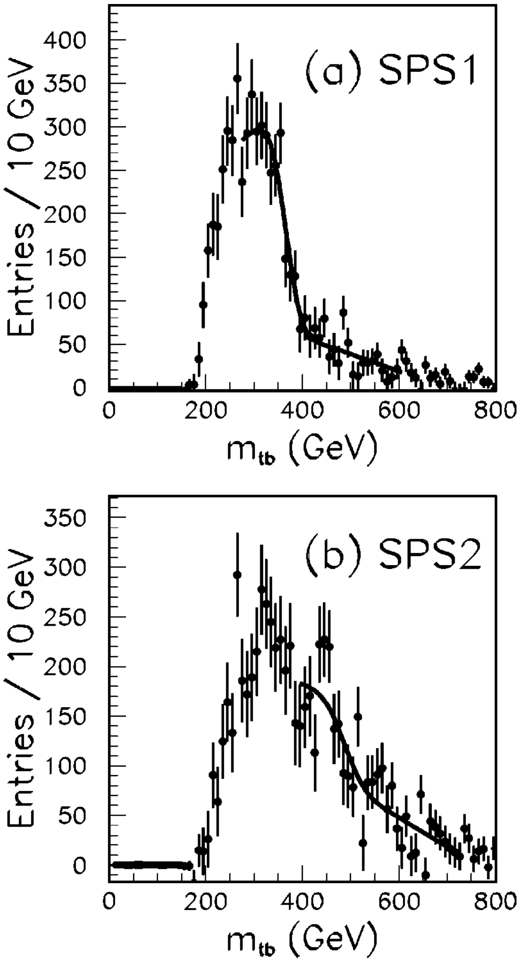

FIG. 13. The m_{tb} distributions at (a) SPS 1 and (b) SPS 2. The fit curves are also shown.

At SPS 5, the stop is so light that the decay $\tilde t_1 \to b\tilde\chi_1^\pm$ is kinematically closed. The gluino decay branching ratio into $\tilde b_1$ is large (9%), but the $\tilde b_1$ subsequently decays mostly into $W\tilde t_1$ (80%). We thus do not find any significant edge.

SPS 4 is an example that a straightforward application of our reconstruction technique fails to find $M_{tb}^{\rm w}$. The distribution is shown in Fig. 14. The sbottom is light because of large $\tan\beta$, and the dominant gluino decay mode is $\tilde g \to b\tilde b_1$ (78%). The sbottom further decays into a chargino (36%) or the second lightest neutralino (30%). Decays of the chargino and second lightest neutralino are dominated by

---

[3] However, $\Delta\chi^2$ is sometimes large even when decay mode (III) dominates the distribution. For example, $\Delta\chi^2=41.4$ for point A1.

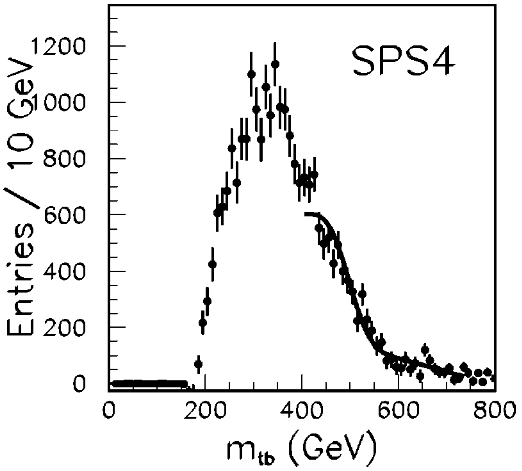

FIG. 14. The m_{tb} distribution at SPS 4. The fit curve is also shown.

$\tilde{\chi}_1^\pm \to W\tilde{\chi}_1^0$ (100%) and $\tilde{\chi}_2^0 \to Z^0\tilde{\chi}_1^0$ (98%), respectively. The dominance of the decay into Z^0 or W is common when decay into the Higgs boson or sleptons is kinematically forbidden. Some of the decays $\tilde{g} \to b\tilde{b} \to bb\tilde{\chi}_2^0$ are reconstructed as tb events together with additional gauge bosons, resulting in the m_{tb} distribution having a quasi-edge structure. The edge is reconstructed by our fit (see Table VII). Note that the end point of the m_{bb} distribution of the decay is 403 GeV, while the reconstructed m_{tb} distribution of the events with decay $(\mathrm{I})_2$ has a peak around 500 GeV and the distribution ends around 580 GeV, close to the kinematical limit $m_{\tilde{g}} - m_{\tilde{\chi}} \sim 600$ GeV. The edge structure is identified as that of mode $(\mathrm{I})_2$ with a tagged $Z^0 \to ll$. In the m_{tb} distribution, the second edge structure from decay mode (III) or (IV) is weakly seen in the distribution. Assuming that two edges exist, we find the second end point $M_{tb}^{\mathrm{fit}} = 425.4 \pm 15.2$ GeV and $h = 349.4 \pm 74.4/(10\ \mathrm{GeV})$.

IV. EVENTS WITH ADDITIONAL TAGS

At the points given in Table I, the lighter chargino and neutralinos (inos) $\tilde{\chi}_1^\pm$, $\tilde{\chi}_1^0$, and $\tilde{\chi}_2^0$ are gaugino-like, while the heavier inos $\tilde{\chi}^h \equiv \tilde{\chi}_2^\pm$, $\tilde{\chi}_3^0$, and $\tilde{\chi}_4^0$ are Higgsino-like. Unlike the first and second generation squarks, the third generation squarks can decay into the heavier inos. This is because the third generation squarks couple to the Higgsinos by top (or bottom) Yukawa coupling. Identification of the cascade decay chain $\tilde{g} \to \tilde{t}/\tilde{b} \to \tilde{\chi}^h$ is a probe for the supersymmetric version of Yukawa interactions. In addition, the decay distribution may be sensitive to the mass difference $m_{\tilde{g}} - m_{\tilde{\chi}^h} \sim M_3 - \mu$.

TABLE VIII. Some of the chargino and neutralino branching ratios in percent at point C.

Decay mode	Br in %	Decay mode	Br in %
$\tilde{\chi}_2^\pm \to W\tilde{\chi}_2^0$	29	$\tilde{\chi}_3^0 \to W\tilde{\chi}^\pm$	59
$\tilde{\chi}_2^\pm \to Z^0\tilde{\chi}_1^\pm$	26	$\tilde{\chi}_3^0 \to Z^0\tilde{\chi}_1^0$	1.7
$\tilde{\chi}_2^\pm \to l\tilde{\nu}$	3.0	$\tilde{\chi}_3^0 \to Z^0\tilde{\chi}_2^0$	25
$\tilde{\chi}_2^\pm \to \nu\tilde{l}$	6.8		
$\tilde{\chi}_4^0 \to W\tilde{\chi}_1^\pm$	59	$\tilde{\chi}_2^0 \to l\tilde{l}_L$	9.8
$\tilde{\chi}_4^0 \to Z^0\tilde{\chi}_1^0$	1.7	$\tilde{\chi}_2^0 \to l\tilde{l}_R$	3.0
$\tilde{\chi}_4^0 \to Z^0\tilde{\chi}_2^0$	1.3	$\tilde{\chi}_1^\pm \to W\tilde{\chi}_1^0$	11
$\tilde{\chi}_4^0 \to l\tilde{l}_L$	3.0	$\tilde{\chi}_1^\pm \to l\tilde{\nu}_L$	37
$\tilde{\chi}_4^0 \to l\tilde{l}_R$	0.9	$\tilde{\chi}_1^\pm \to \nu\tilde{l}_L$	8.9

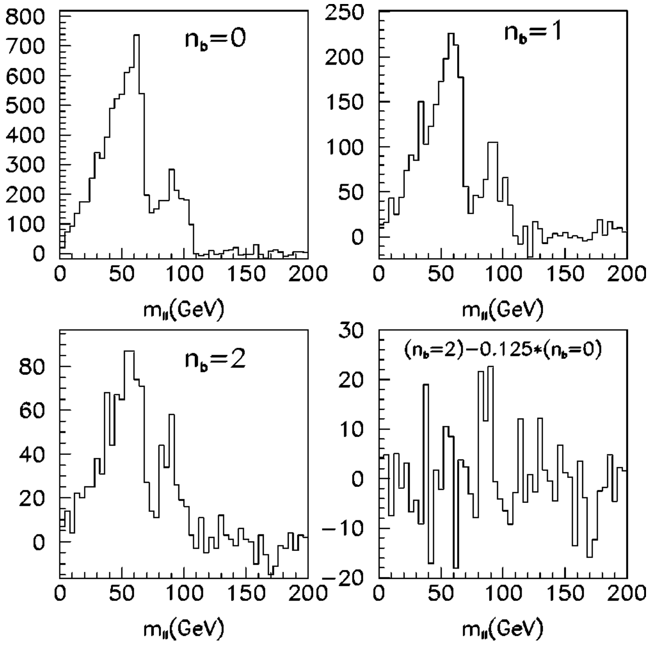

FIG. 15. Distributions of $m_{e^+e^-} + m_{\mu^+\mu^-} - m_{e^+\mu^-} - m_{e^-\mu^+}$ with $n_b = 0$ (top left), 1 (top right), 2 (bottom left). The bottom-right plot shows the distribution for $n_b = 2$ after subtracting the scaled distribution for $n_b = 0$ by a factor of $\sim 1/8$.

In this section we show an example to select such events by requiring additional leptons in the final state. We study point C, where the stop and sbottom decay into $\tilde{\chi}^h$ with large branching fractions. At this point the gluino decay branching ratios are $\mathrm{Br}(\tilde{g} \to \tilde{t}_1) = 15.1\%$ and $\mathrm{Br}(\tilde{g} \to \tilde{b}_1) = 14\%$. The squarks further decay into the Higgsino-like inos with branching ratios of $\mathrm{Br}(\tilde{b}_1 \to \tilde{\chi}^h) = 24\%$ and $\mathrm{Br}(\tilde{t}_1 \to \tilde{\chi}^h) = 13\%$, respectively. The stop and sbottom decay branching ratios are comparable to those into $\tilde{\chi}_1^\pm$.

Some of the decay branching ratios of the charginos and neutralinos are listed in Table VIII. The Higgsino-like inos have large branching ratios into the Z^0 boson. The heavier inos also have non-negligible branching ratios into triple leptons, because they may also decay into $\tilde{\chi}_2^0$ which further decays into leptons.

The signature of the heavier inos from stop or sbottom is an excess of the Z^0 boson or three leptons in events with two b jets. In Fig. 15 we plot the invariant mass of the same-flavor opposite-sign leptons (m_{ll}) for events with $n_b = 0$, 1, and 2, where n_b is the number of b jets in an event. In the plots, accidental lepton pair distributions estimated with events with different-flavor opposite-sign leptons are sub-

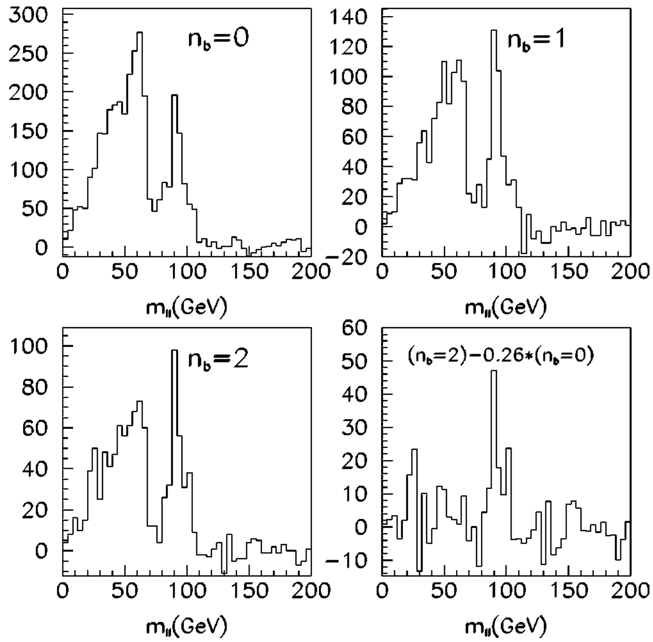

FIG. 16. Same as Fig. 15, but for events with three leptons.

tracted. All plots show a common structure that the invariant mass distribution increases toward the edges around 70 GeV and 105 GeV, which correspond to the decay chains of $\tilde{\chi}_2^0 \to l\tilde{l}_L \to ll\tilde{\chi}_1^0$ and $\tilde{\chi}_2^0 \to l\tilde{l}_R \to ll\tilde{\chi}_1^0$, respectively. The Z^0 peak is also seen in the plots. As n_b increases, the Z^0 peak height becomes more significant relative to the edge structure. The excess of $Z^0 \to ll$ in the $n_b=2$ sample indicates the Z^0 boson originating primarily from stop or sbottom. The difference of the decay patterns of sbottom and stop and the first generation squarks may be studied by comparing the heights of m_{ll} edges and Z^0 peak. For point C, the edges in the m_{ll} distribution for the $n_b=2$ sample are completely subtracted by the distribution for the $n_b=0$ sample scaled by a factor of $\sim 1/8$, and the Z^0 peak remains (the bottom-right plot of Fig. 15).

The same analysis can be performed by using events with three leptons. In Fig. 16 we plot the sum of invariant mass distributions $m_{e^+e^-}+m_{\mu^+\mu^-}-m_{e^+\mu^-}-m_{e^-\mu^+}$ for all possible combinations of opposite-sign lepton pairs. In this mode the Z^0 peak is more significant. The ratio of edge heights in the m_{ll} distribution for the $n_b=2$ sample to that of the $n_b=0$ sample is $\sim 1/4$. This means that events originating from the decay $\tilde{b}/\tilde{t} \to \tilde{\chi}^h$ dominate the three-lepton events and events with $n_b=0$ arise due to misidentified b jets.

Note that these plots at point C are made for a total of 3×10^6 SUSY events, which corresponds to an integrated luminosity of 600 fb^{-1}. The statistics for 100 fb^{-1} is not significant. However, this procedure should be useful for a lighter mass spectrum where decay of the third generation squarks to $\tilde{\chi}^h$ is open.

After establishing the contribution of the decay $\tilde{t}/\tilde{b} \to \tilde{\chi}^h$ in the tagged $bb3l$ and bbZ^0 events, we may reconstruct the tb system in the sample. The tb reconstruction is similar to that described in Sec. II, except that the distributions are made without the cuts for the effective mass and lepton, because the standard model background is expected to be small now. In Fig. 17 the m_{tb} distribution with tagged three leptons is shown. The number of events after sideband subtraction is 242.5. The m_{tb} distribution is concentrated just below the expected end point which is close to $m_{\tilde{g}}-m_{\tilde{\chi}_2^\pm}$ $\sim$400 GeV, although the statistics is low. The distribution of tagged $Z^0 \to ll$ is similar, and the number of events after sideband subtraction is 142.

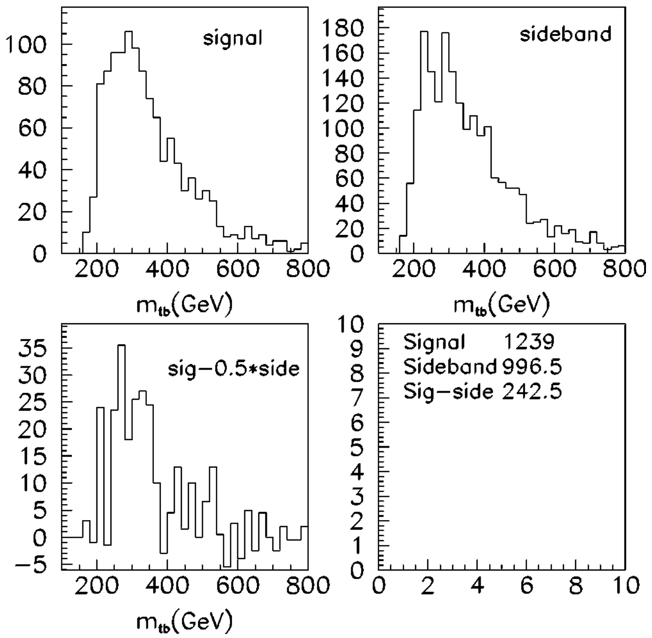

FIG. 17. The m_{tb} distributions for events with tagged three leptons. Top left: signal distribution. Top right: background estimated by sideband events. Bottom left: distribution after sideband subtraction.

V. STOP AND SBOTTOM PROPERTIES IN THE MSUGRA MODEL

In this section we interpret our study of the third generation squarks at the LHC in a framework of the MSUGRA model. The LHC may determine the MSUGRA parameters m_0, $M_{1/2}$, A_0, and $\tan\beta$ through measurement of various distributions. The decay chains $\tilde{q} \to q\tilde{\chi}_2^0$ followed by $\tilde{\chi}_2^0 \to h\tilde{\chi}_1^0$, $Z^0\tilde{\chi}_1^0$, $l\tilde{l}$, or $ll\tilde{\chi}_1^0$ are especially useful if the kinematical end points of the distributions are measured. The effective mass measurement of the inclusive SUSY signal is also useful to determine the absolute SUSY scale. Among these parameters, the A_0 parameter is only weakly constrained. This is because the left-right mixings of sbottom and stau are almost fixed by $\mu\tan\beta$, and A_t is insensitive to A_0 as will be described below. One of the possible ways to determine A_0 is to measure the mass difference between squarks or sleptons with different flavors, which is caused by the renormalization group equation (RGE) running between the GUT scale and the weak scale.

The squark mass matrix is given as

$$-\mathcal{L}_{\rm mass}=\begin{pmatrix}\tilde{f}_L^\star & \tilde{f}_R^\star\end{pmatrix}\begin{pmatrix}m_{LL}^2 & m_{LR}^2\\ m_{LL}^2 & m_{RR}^2\end{pmatrix}\begin{pmatrix}\tilde{f}_L\\ \tilde{f}_R\end{pmatrix}, \tag{10}$$

where

$$m_{LL}^2=m_{\tilde{t}_L}^2+m_t^2+m_Z^2\cos 2\beta\left(\frac{1}{2}-\frac{2}{3}\sin^2\theta_W\right),$$

$$m_{RR}^2=m_{\tilde{t}_R}^2+m_t^2+\frac{2}{3}m_Z^2\cos 2\beta\sin^2\theta_W,$$

$$m_{LR}^2=m_t(A_t-\mu\cot\beta), \tag{11}$$

for stops, and

$$m_{LL}^2=m_{\tilde{t}_L}^2+m_b^2+m_Z^2\cos 2\beta\left(-\frac{1}{2}+\frac{1}{3}\sin^2\theta_W\right),$$

$$m_{RR}^2=m_{\tilde{b}_R}^2+m_b^2-\frac{1}{3}m_Z^2\cos 2\beta\sin^2\theta_W,$$

$$m_{LR}^2=m_b(A_b-\mu\tan\beta), \tag{12}$$

for sbottoms.

In the MSUGRA, the SUSY breaking parameters at the weak scale in these mass matrices are evaluated by the RGEs with the universal GUT scale boundary conditions. When the bottom-Yukawa coupling is negligible, it is convenient to present the SUSY breaking parameters by the infrared-fixed point value for the top-Yukawa coupling constant $\overline{y_f}$ [19]:

$$\overline{y_f}=\frac{F'(t)}{6F(t)}. \tag{13}$$

Here,

$$F(t)=\int_0^t dt'\left(\frac{\alpha_3(t)}{\alpha_{GUT}}\right)^{16/9}\left(\frac{\alpha_2(t)}{\alpha_{GUT}}\right)^{-3}\left(\frac{\alpha_1(t)}{\alpha_{GUT}}\right)^{-13/99}, \tag{14}$$

where $t=1/(4\pi)\log\mu^2/M_{GUT}^2$ and μ is the renormalization scale. α_{GUT} is the gauge coupling constant at the GUT scale. The SUSY breaking parameters for the third generation at the low-energy scale are approximately given using the value as

$$m_{\tilde{t}_L}^2\simeq 0.7M_{\tilde{g}}^2+0.5m_0^2-(0.16A_0^2-0.25A_0M_{\tilde{g}})(1-\xi),$$

$$m_{\tilde{t}_R}^2\simeq 0.5M_{\tilde{g}}^2+m_0^2(1-\xi)-(0.33A_0^2-0.51A_0M_{\tilde{g}})(1-\xi),$$

$$m_{\tilde{b}_R}^2\simeq m_0^2+0.8M_{\tilde{g}}^2,$$

$$A_t\simeq -0.7M_{\tilde{g}}+A_0(1-\xi),$$

$$A_b\simeq -1.2M_{\tilde{g}}+0.8A_0, \tag{15}$$

up to $\mathcal{O}((1-\xi)^2)$, where

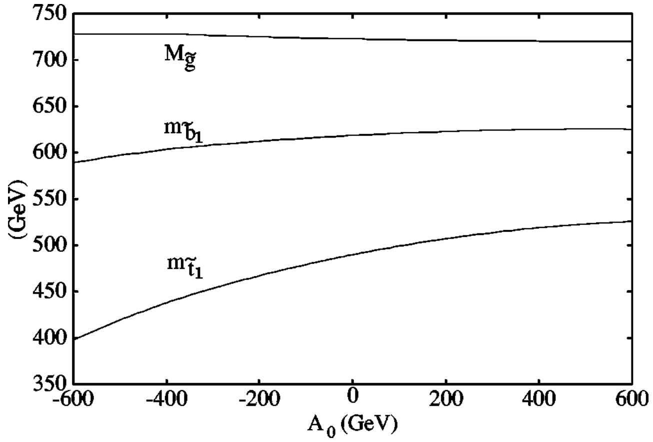

FIG. 18. Masses for $\tilde{g}$, $\tilde{t}_1$, and $\tilde{b}_1$ as functions of A_0. Here, $m_0=230$ GeV, $M_{1/2}=300$ GeV, $\tan\beta=30$, and $\mu>0$.

$$\xi(\equiv y_t^2/\overline{y_t^2})=\left(\frac{m_t}{203\sin\beta({\rm GeV})}\right)^2. \tag{16}$$

Here we use the GUT relation for the gaugino masses, $M_{\tilde{g}}\simeq 2.8M_{1/2}$. For the pole top mass $m_t^{pole}=175$ GeV, ξ ranges $0.7\lesssim\xi\lesssim 0.9$.

From Eq. (15), the qualitative behavior of the SUSY breaking parameters is clear. The reduction of the $m_{\tilde{t}_L}^2$ and $m_{\tilde{t}_R}^2$ is more efficient for $A_0M_{\tilde{g}}<0$, although the dependence is suppressed by an overall factor of $1-\xi$. The right-handed stop mass $m_{\tilde{t}_R}$ is also insensitive to m_0. In a moderate $\tan\beta$ region, $\tilde{t}_1$ and $\tilde{b}_1$ is almost right handed and left handed, respectively.

In Fig. 18 we show the masses of $\tilde{g}$, $\tilde{t}_1$, and $\tilde{b}_1$ as functions of A_0, where the other MSUGRA parameters are fixed to $m_0=230$ GeV, $M_{1/2}=300$ GeV, $\tan\beta=10$, and $\mu>0$. As expected from the discussion above, the masses $m_{\tilde{t}_1}$ and $m_{\tilde{b}_1}$ have sensitivity to A_0. The reduction of $m_{\tilde{t}_L}^2$ and $m_{\tilde{t}_R}^2$ by the top-Yukawa coupling constant is larger when $A_0<0$.

The stop $\tilde{t}_1$, which is almost $\tilde{t}_R$, is lighter than the gluino unless m_0 is very large. Similarly, since the sbottom $\tilde{b}_1$ is almost $\tilde{b}_L$, the branching ratio to the edge events in Eq. (1), which includes $\tilde{\chi}_1^\pm$, is large since it has SU(2) gauge and top-Yukawa interactions. The study of the edge events has therefore potentially high feasibility in the MSUGRA. Figure 19 shows the regions where the gluino decays into $t\tilde{t}_1$ and $b\tilde{b}_1$ are open in a plane of m_0 and A_0. In this plot the other parameters are fixed to $m_{\tilde{g}}=707$ GeV, $\tan\beta=5$ or 30, and $\mu>0$.

Since the top quark mass deviates from the fixed-point value, the A_0 dependence on $m_{\tilde{t}_L}^2$ and $m_{\tilde{t}_R}^2$ survives, as shown in Fig. 18. This may lead to a measurable dependence on A_0 of the end point of the m_{tb} distribution. In Fig. 20(a), we show $M_{tb}^{\rm w}$, $M_{tb}({\rm III})_1$, and $M_{tb}({\rm IV})_{11}$ as functions of A_0. Since $\tilde{b}_1$ is heavy, $M_{tb}({\rm IV})_{11}$ is lower than $M_{tb}({\rm III})_1$. However, ${\rm Br}(\tilde{g}\to t\tilde{t}_1)$ is larger than ${\rm Br}(\tilde{g}\to b\tilde{b}_1)$ due to the phase

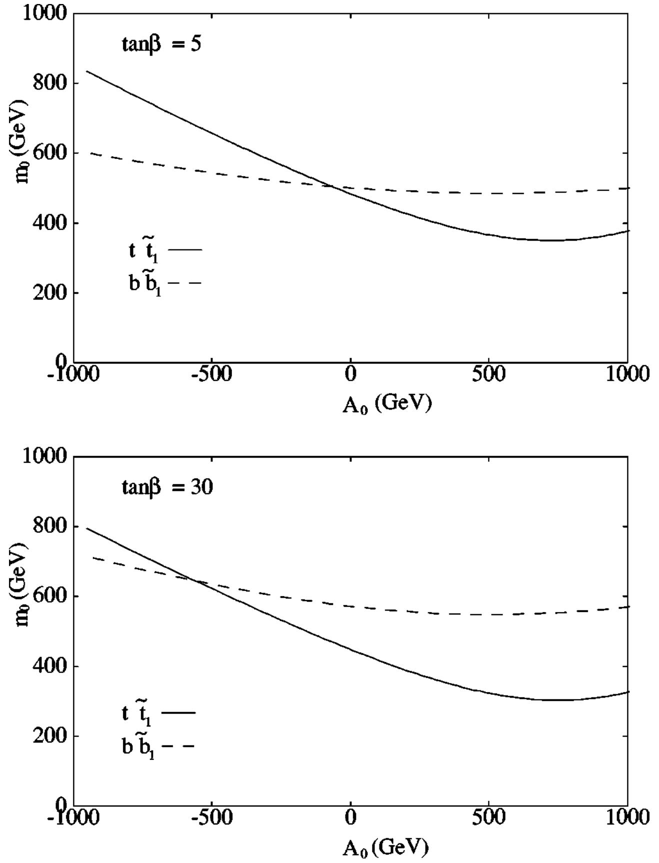

FIG. 19. Contours where $m_{\tilde{g}}=m_{\tilde{t}_1}+m_t$ and $m_{\tilde{b}_1}+m_b$ on a plane of m_0 and A_0. The gluino decays into $t\tilde{t}_1$ and $b\tilde{b}_1$ are open below the contours. Here, $m_{\tilde{g}}=707$ GeV, $\tan\beta=5$ and 30, and $\mu>0$.

space, which makes M_{tb}^{w} closer to $M_{tb}(\mathrm{III})_1$. If M_{tb}^{w} is determined with a precision of a few percent as in our simulation study, the A_0 parameter can be evaluated with a precision of ~ 50 GeV.

In addition to the weighted end point M_{tb}^{w}, the edge height h of the m_{tb} distribution is measurable, and the height is roughly proportional to the branching ratio of the gluino to edge events arising from the decay modes (III) and (IV) in Eq. (1). In Sec. III D we proposed to investigate $N_{\mathrm{fit}}/N_{\mathrm{all}}$ where N_{fit} is the number of the edge event estimated by the fit and N_{all} is the total tb events selected. It is related to the normalized branching ratio $\mathrm{Br(edge)}/\mathrm{Br}(\tilde{g}\rightarrow bbX)$. The normalized branching ratio is sensitive to the branching ratios for $\tilde{t}_1$ and $\tilde{b}_1$, and the uncertainty in fragmentation and b tagging efficiency would be canceled out in the ratio.

In Fig. 20(b) we show the branching ratio $\mathrm{Br}(\tilde{g}\rightarrow bbX)$ and the branching ratio of the gluino to the edge events normalized by $\mathrm{Br}(\tilde{g}\rightarrow bbX)$. They are decreasing functions of A_0, since the $\tilde{t}_1$ and $\tilde{b}_1$ is heavier for larger A_0. While the behavior of $\mathrm{Br}(\tilde{g}\rightarrow bbX)$ is moderate, the normalized branching ratio of the edge events is sensitive to A_0, since it depends on the branching ratios of $\tilde{t}_1$ and $\tilde{b}_1$. In Fig. 20(b) the normalized branching ratio has two kinks, where some decay modes for $\tilde{t}_1$ or $\tilde{b}_1$ are open. The first kink around $A_0\sim -500$ GeV comes from a change of the branching ratio of $\tilde{t}_1$. The dominant decay modes of $\tilde{t}_1$ are $b\tilde{\chi}_1^{\pm}$ and $t\tilde{\chi}_1^0$; however, mode $t\tilde{\chi}_2^0$ is open around $A_0\sim -500$ GeV. The decay modes $\tilde{t}_1\rightarrow b\tilde{\chi}_2^{\pm}$ and $\tilde{b}_1\rightarrow t\tilde{\chi}_2^{\pm}$ are open at the second kink around $A_0\sim -150$ GeV. The decay modes are not included in the edge events, because the end point $M_{tb}(\mathrm{III})_2$ is significantly lower than $M_{tb}(\mathrm{III})_1$. The additional tags for $\tilde{\chi}_2^{\pm}$ discussed in the previous section to identify the decay work for the region. Since $\tilde{\chi}_2^{\pm}$ is Higgsino-like and the Yukawa coupling to $\tilde{b}_1$ is enhanced by the top-Yukawa coupling, the decay mode $\tilde{b}_1\rightarrow t\tilde{\chi}_2^{\pm}$ becomes dominant for $A_0>-150$ GeV, and then the normalized branching ratio becomes quickly diluted.

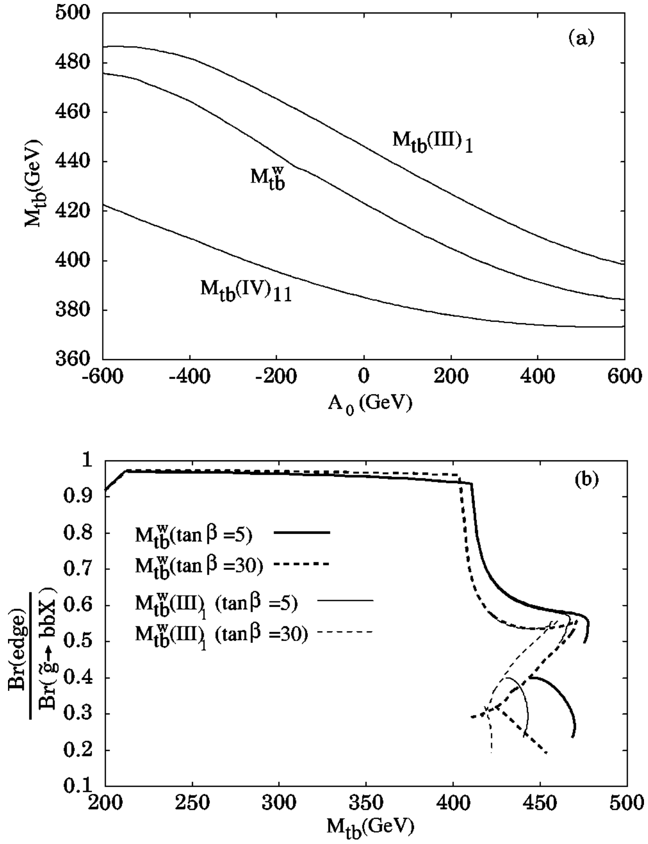

FIG. 20. (a) M_{tb}^{w}, $M(\mathrm{III})_1$, and $M(\mathrm{IV})_{11}$ as functions of A_0. (b) $\mathrm{Br}(\tilde{g}\rightarrow bbX)$ and $\mathrm{Br(edge)}/\mathrm{Br}(\tilde{g}\rightarrow bbX)$ as functions of A_0. Input parameters are the same as in Fig. 18.

In the MSUGRA model, the masses of $\tilde{t}_1$ and $\tilde{b}_1$ are related to each other in a broad parameter space. As the determination of $m_{\tilde{b}_1}$ has been studied in Ref. [2], we now discuss M_{tb}^{w} and the normalized branching ratio with a fixed $m_{\tilde{b}_1}$ value. We fix $m_{\tilde{b}_1}=570$ GeV and $M_{\tilde{g}}=707$ GeV for $\tan\beta=5$ and 30, and show M_{tb}^{w} $[M_{tb}(\mathrm{III})_1]$ as a function of $m_{\tilde{t}_1}$ in Fig. 21(a). Our parameter scan is restricted to the range $|A_0|<2$ TeV.

We have two disconnected solutions corresponding to -1400 (-1850) GeV$<A_0<-280$ (470) GeV and 1350 (1600) GeV$<A_0<2000$ GeV for $\tan\beta=5$ (30), respectively.

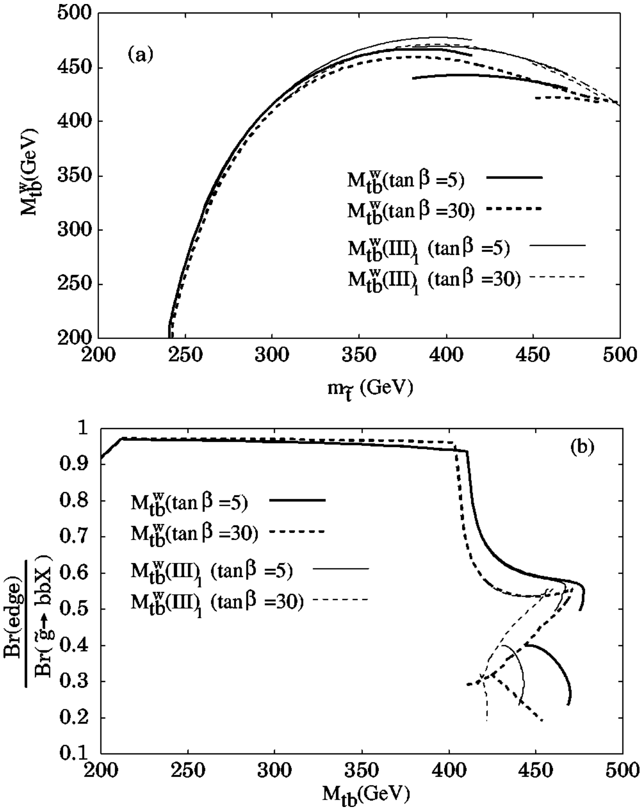

FIG. 21. For fixed $m_{\tilde{b}_1}=570$ GeV and $M_{\tilde{g}}=707$ GeV, (a) $M_{tb}^{\rm w}$ and $m_{\tilde{t}_1}$ and (b) $M_{tb}^{\rm w}$ $[M_{tb}(\mathrm{III})]$ and Br(edge)/Br$(\tilde{g}\to bbX)$. Here, -2 TeV$<A_0<2$ TeV, $\tan\beta=5$ and 30, and $\mu>0$. m_0 is fixed by $m_{\tilde{b}_1}$. The neutralino LSP is assumed.

The A_0 region between the two solutions is not allowed because of the experimental constraint of $\tilde{\tau}$ mass or charged LSP. For $\tan\beta=5$ (30), m_0 is smaller than 460 (750) GeV for $A_0<0$ and 500 (300) GeV for $A_0>0$. Since $\tilde{b}_1\sim\tilde{b}_L$ in the MSUGRA model, a larger $|A_0|$ corresponds to a larger m_0 for a fixed $m_{\tilde{b}_1}$, as expected from Eq. (15). Nevertheless, $\tilde{t}_1$ could be much lighter than $\tilde{b}_1$ for a large and negative value of A_0 as can be seen in Fig. 21(a).[4] Note that $M_{tb}^{\rm w}$ is determined for a fixed $\tilde{t}_1$ mass when $m_{\tilde{t}_1}$ is lighter than 370 GeV. If $m_{\tilde{b}_1}$ is constrained elsewhere, $m_{\tilde{t}_1}$ is strongly restricted by the $M_{tb}^{\rm w}$ measurement under the MSUGRA assumption.

In Fig. 21(b) we show the solution in a $M_{tb}^{\rm w}$ and Br(edge)/Br$(\tilde{g}\to bbX)$ plane. The normalized branching ratio is almost 1 for $M_{tb}^{\rm w}<400$ GeV (or $m_{\tilde{t}_1}<300$ GeV). When the mass difference of $m_{\tilde{t}_1}$ and $m_{\tilde{b}_1}$ is large, the decay of $\tilde{b}_1$ is dominated by $W\tilde{t}_1$. Furthermore, for $m_{\tilde{t}_1}\lesssim 300$ GeV, Br$(\tilde{t}_1\to b\tilde{\chi}_1^{\pm})$ is 100%. However, since $m_{\tilde{q}}>m_{\tilde{g}}$ in this region, squark and gluino production goes to the final states having four bottom quarks, where we have seen the disagreement between the measurement $N_{\rm edge}/N_{\rm all}$ and Br(edge)/Br$(\tilde{g}\to bbX)$ in Sec. III D. In this case our study must be extended to events with more than three tagged b jets.

Note that the decay $\tilde{\chi}_2^0\to\tilde{l}$ is mostly closed in Fig. 21. The decay is open only at the rightmost region of Fig. 21(b), near the end of the lines of the solutions. If this decay is open, the masses of $\tilde{q}$, $\tilde{l}$, and $\tilde{\chi}_1^0$ are model independently determined by the m_{ll}, m_{llj}, and m_{lj} distributions. When this decay mode is kinematically forbidden, one needs to combine various distributions for a consistency check of the MSUGRA assumptions. As is already shown in Fig. 19, the decay $\tilde{g}\to\tilde{b}/\tilde{t}$ is open up to $m_0\sim m_{\tilde{g}}$, providing information on the third generation squarks in a wide region of parameter space.

VI. MEASUREMENT OF TOP POLARIZATION

Similar to tau-lepton decay, we may measure the polarization of the top quark since it decays to bW via the $(V\text{-}A)$ interaction. Top quarks from the $\tilde{g}$, $\tilde{t}$, and $\tilde{b}$ decays are polarized, and the polarization depends on the mixing angles for stops, charginos, and neutralinos.

The bottom quark angular distribution in the polarized top quark decay is

$$\frac{1}{\Gamma_t}\frac{d\Gamma_t}{d\cos\theta}\propto\left(\frac{m_t}{m_W}\right)^2\sin^2\frac{\theta}{2}+2\cos^2\frac{\theta}{2}, \tag{17}$$

where θ is the angle between the direction of the bottom quark and the direction of the top quark spin in the rest frame of the top quark. The terms proportional to $(m_t/m_W)^2$ come from the decay to the longitudinal W boson. The bottom quark thus tends to go to an opposite direction that of the top quark spin.

In decay mode $(\mathrm{III})_1$, the top quark from a gluino decay is polarized to be left handed (right handed) if $\tilde{t}_1$ is left handed (right handed). The polarization is reflected on the invariant mass distribution of the bb system (m_{bb}) if the top quark is relativistic enough in the gluino rest frame. Here, one of the bottom quarks comes from the top quark decay and the other comes from $\tilde{t}_1\to b\tilde{\chi}^{\pm}$. Especially, when the invariant mass m_{tb} is close to the end point M_{tb} of decay mode $(\mathrm{III})_1$, the top and bottom quarks go to the opposite direction to each other in the gluino rest frame. Thus, the distribution of the invariant mass m_{bb} for events with m_{tb} close to $M_{tb}(\mathrm{III})_1$ is harder (softer) for left-handed (right-handed) top quarks.

In Fig. 22 we show the m_{bb} distribution from decay chain $(\mathrm{III})_1$. In this simulation, we use the HERWIG generator, since it respects helicities for each particle in the processes. We generated a large number of events which go through decay $(\mathrm{III})_1$. We use the mass spectrum at reference point A1 in Table I. We use events with 400 GeV$<m_{tb}<$470 GeV to make the distribution, and the solid (dotted) line is for the left-handed (right-handed) stop. The statistical significance

---

[4] $|A_0|<3m_0$ for $A_0<0$, satisfying a condition for a consistent minimum for the potential.

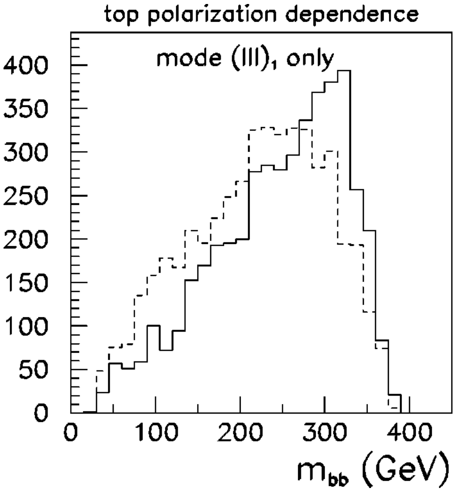

FIG. 22. Distribution of m_{bb} in decay chain (III)$_1$. The (dashed) line is for $\tilde{t}_1 = \tilde{t}_L(\tilde{t}_R)$ and 400 GeV$<m_{tb}<$470 GeV. We use the mass spectrum in the sample point A1 in Table I, and the normalization is arbitrary.

in the difference between the left-handed and right-handed stops is about 3σ for $\mathcal{O}(100)$ events.

In the above simulation, we neglect the contributions of other decay chains such as (III)$_{11}$ and (IV)$_{11}$. The other decay chains may contribute to the m_{bb} distribution even if we impose that m_{tb} be near the end point. The m_{bb} distributions in modes (III)$_{11}$ and (IV)$_{11}$ do not depend on the polarization for the top quark, since the top quark distribution in the scalar boson decay is spherical. In Fig. 23 we show the m_{tb} distribution around the edge region at reference point A1. The solid line is for the total distribution, the dashed line is for the distribution excluding mode (III)$_1$, and the dotted line is for the distribution excluding modes (III)$_1$, (III)$_{11}$, and (III)$_{21}$. About half of the events near the end point come from signal mode (III)$_1$, and the ratio between the signal events and the rest depends on the MSSM parameters.

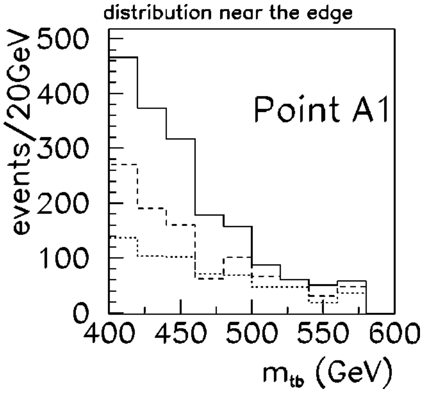

FIG. 23. The solid line is for the total m_{tb} distribution at sample point A1, the dashed line is for the m_{tb} distribution excluding mode (III)$_1$, and the dotted line is for the m_{tb} distribution excluding modes (III)$_1$, (III)$_{11}$, and (III)$_{21}$.

VII. CONCLUSIONS

In this paper we study the cascade decays $\tilde{g} \rightarrow (t\tilde{t}_1 \text{ or } b\tilde{b}_i) \rightarrow tb\tilde{\chi}_i^{\pm}$ at the LHC by reconstructing the tb final state where the top quark decays hadronically. The m_{tb} distribution of the cascade decay has an edge structure. The measurement of the end point and the edge height of the m_{tb} distribution constrains a combination of the masses of $\tilde{g}$, $\tilde{b}$, $\tilde{t}$, and $\tilde{\chi}^{\pm}$ and the decay branching ratios of the particles involved in the decays.

Through a detailed simulation study, we show in this paper that measurement of the end point and edge height on a continuum background is indeed possible. Namely, the end point of the cascade decay calculated in the parton level agrees with the reconstructed edge position, and the ratio of N_{edge} (the number of reconstructed edge events) and N_{all} (the number of total reconstructed tb events) is understood well by the ratio $\text{Br(edge)}/\text{Br}(\tilde{g} \rightarrow bbX)$.

The end point and branching ratios depend on the mass and left-right mixing of the $\tilde{t}$ and $\tilde{b}$, as well as the chargino and neutralino masses and mixings in the MSSM. In the MSUGRA model, these sparticle spectra are expressed by a few parameters at the GUT scale. The decay mode $\tilde{g} \rightarrow (t\tilde{t}_1 \text{ or } b\tilde{b}_i) \rightarrow tb\tilde{\chi}_1^{\pm}$ is open for a wide region of parameter space where $m_0 < m_{\tilde{g}}$. The m_{tb} distribution is sensitive to the A_0 parameter, the trilinear coupling at the GUT scale. The distribution is most sensitive to A_0 when $A_0 M_{1/2} < 0$.

The stop and sbottom could decay into both heavier and lighter charginos and neutralinos unlike first and second generation squarks. This is because third generation squarks have a large top (bottom-)Yukawa coupling to the Higgsinos. A strategy to search for such decays specific to the stop and sbottom is described in Sec. VI. The Yukawa coupling is also related to the $\tilde{t}_L$-$\tilde{t}_R$ mixing. The polarization of the top quark arising from the gluino decay $\tilde{g} \rightarrow t\tilde{t}$ depends on the stop left-right mixing. The dependence of the m_{bb} distribution on the top polarization in the tagged tb sample is discussed in Sec. VI.

To understand the event distribution better, one needs to know the nature of the quark and gluon fragmentations into jets. The reconstruction efficiencies are significantly different between the two standard SUSY generators HERWIG and PYTHIA, which adopt different models for the fragmentation. We point out that the smearing of the jet pair invariant mass originating from a W decay affects the reconstruction efficiency.

The interplay between the LHC and future LC would be useful to reduce the systematics coming from the uncertainties of sparticle masses and decay branching ratios. They would be reduced dramatically if some of the charginos and neutralinos are accessible at the LC. Model-independent and precise determination of the stop and sbottom masses may be possible in such cases and will be discussed elsewhere.

ACKNOWLEDGMENTS

We thank the ATLAS Collaboration for useful discussion. We have made use of the physics analysis framework and

TABLE IX. Fit results at point A1. We use the cone-based algorithm or the K_T algorithm with cone sizes of $R=0.4,0.5,0.6$. The fit is based on 3×10^6 events. The M_{tb}^{w} is 459 GeV.

Gen	Jet	M_{tb}^{fit}[GeV]	h/(10 GeV)
PY	cone 0.4	455.2±8.2	271.4±22.7
	0.5	436.1±7.7	272.9±33.4
	0.6	461.1±10.4	217.8±22.8
	K_T 0.4	442.0±4.7	321.3±22.3
	0.5	452.2±6.0	305.3±21.3
	0.6	459.1±6.1	241.6±31.6
HW	cone 0.4	434.5±5.8	354.8±23.3
	0.5	460.2±4.9	349.2±22.8
	0.6	440.9±7.1	305.3±33.7
	K_T 0.4	434.9±4.3	406.5±22.1
	0.5	460.0±5.5	379.6±33.5
	0.6	468.4±5.8	314.3±20.7

tools which are the result of collaboration-wide efforts. We especially thank Dr. J. Kanzaki and D. Toya. We acknowledge ICEPP, University of Tokyo, for providing us computing resources. This work is supported in part by a Grant-in-Aid for Science Research, Ministry of Education, Science and Culture, Japan (No. 13135297 and No. 14046225 for J.H., No. 11207101 for K.K., and No. 14540260 and No. 14046210 for M.M.N.).

APPENDIX: RELIABILITY OF SIDEBAND SUBTRACTION

In this paper, we generate events both by the PYTHIA and HERWIG generators. The HERWIG generator uses a parton-shower approach for initial- and final-state QCD radiations including color coherence effects and azimuthal correlation both within and between jets [13]. The full available phase space for the parton shower is restricted to an angular order region; namely, the angle between the two emitted partons is smaller than that of previous branches. On the other hand, the PYTHIA generator adopts the string model [12]. The two generators predict different tb reconstruction efficiencies, which may be considered as the uncertainty in fragmentation.

The definition of jets also affects the number of reconstructed tb events and the reconstruction efficiency. We try two algorithms: a cone-based algorithm and a K_T algorithm (Montreal version), available in the JET Finder Library [20], which is interfaced to the ATLFAST packages.

The cone-based algorithm merges the calorimeter cells around a high-E_T cell in a fixed cone size R. On the other hand, in the K_T algorithm, a cell called a protojet i grows until there are no more protojets j which satisfy $(\Delta\eta)^2+(\Delta\phi)^2<[E_{Ti}^2/\min(E_{Ti}^2,E_{Tj}^2)]R^2$; therefore, the cone size depends on E_T's and the shape of the jet depends on the distribution of the particles in the jet. The K_T algorithm is based on QCD, and it is considered to be advantageous to merge soft jets from an initial parton, although experimentally challenging.

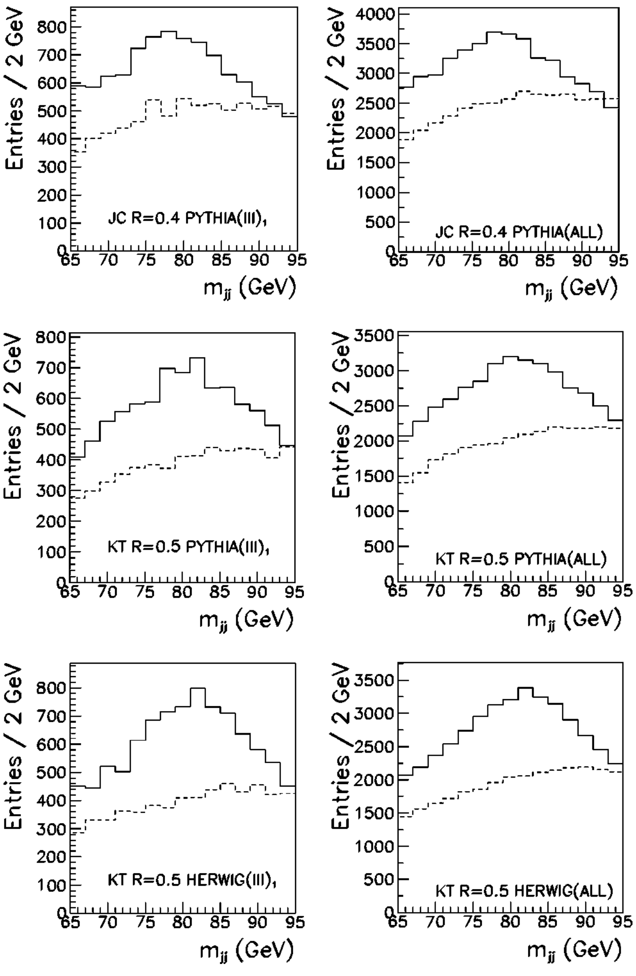

FIG. 24. Distributions of m_{jj} consistent with the W boson mass under the cuts described in Sec. II. The Monte Carlo data are generated for point A1. In the left, we plot events that contain decay chain $\tilde{g}\to t\tilde{t}_1\to tb\tilde{\chi}_1^\pm$ only, while we plot all events in the right. Dotted lines show estimated background. Top figures: PYTHIA with the cone-based algorithm ($R=0.4$). Middle: PYTHIA with the K_T algorithm ($R=0.5$). Bottom: HERWIG with the K_T algorithm ($R=0.5$).

The fit results with different generators and jet finding algorithms at point A1 are summarized in Table IX. The end point M_{tb}^{fit} becomes closer to M_{tb}^{w} as R increases. This is expected because more soft jets are merged to leading jets as R increases. The edge height h is larger for HERWIG with the K_T algorithm. The difference of the height for $R\leqslant0.5$ is more than 25% in Table IX. The height significantly decreases for $R=0.6$. This is because we have to reconstruct a jet pair with relatively small invariant mass ~80 GeV.

To see the origin of the difference more closely, we compare the m_{jj} distributions consistent to the top interpretation in Fig. 24, where the solid histograms are the invariant mass distributions for jet pairs which satisfy $|m_{jj}-m_W|<15$ GeV and $|m_{bjj}-m_t|<30$ GeV. Dashed histograms show the distribution of accidental jet pairs in the W mass region—that is, the "fake W" background—estimated by the sideband method. The left plots are the distributions of the events arising from decay chain $(\mathrm{III})_1$, while the right plots are the m_{tb} distribution of all selected tb events. The distri-

TABLE X. Numbers of events before and after sideband subtraction for events with a gluino that decays through mode $(\mathrm{III})_1$, $\tilde{g}\to t\tilde{t}_1\to tb\tilde{\chi}_1^{\pm}$, and mode $(\mathrm{I})_2$, $\tilde{g}\to b\tilde{b}_1\to bb\tilde{\chi}_2^0$.

		HW		PY	
K_T/cone	R	sig	after sub	sig	after sub
mode $(\mathrm{III})_1$					
cone	0.4	10180	2949	9695	2462
cone	0.5	9659	2974	9213	2447
K_T	0.4	9405	3105	9226	2813
K_T	0.5	9118	3239	8607	2808
mode $(\mathrm{I})_2$					
cone	0.4	2779	574	2630	500
K_T	0.5	2086	448	2058	433

butions at the bottom left (HERWIG and the K_T algorithm for $R=0.5$) are more concentrated around $m_{jj}\sim 80$ GeV compared to the others (PYTHIA and the cone-based or K_T algorithm), corresponding to better reconstruction efficiencies.

Incompleteness of the sideband subtraction is seen in the same figure. Sideband subtraction uses jet pairs with invariant mass $35\ \mathrm{GeV}<m_{jj}<65\ \mathrm{GeV}$ and $95\ \mathrm{GeV}<m_{jj}<125\ \mathrm{GeV}$ to estimate the "fake W" background. On the other hand, as the jets are defined to have $p_T^{jet}>10$ GeV, a jet pair near $m_{jj}\sim 35$ GeV is suppressed. We see an underestimate of background events in the range $65\ \mathrm{GeV}<m_{jj}<70$ GeV, where the dotted line and solid line differ significantly. We find that events with $m_{jj}<70$ GeV do not contribute to the edge structure of the m_{tb} distribution. The events in this region might have to be removed from the candidate events.

The incompleteness of the sideband subtraction can also be seen by comparing the reconstruction efficiency of the events from specific decay chains. Here we take two decay chains for comparison:

$$(\mathrm{III})_1 \quad \tilde{g}\to t\tilde{t}_1\to tb\tilde{\chi}_1^{\pm},$$

$$(\mathrm{I})_2 \quad \tilde{g}\to b\tilde{b}_1\to bb\tilde{\chi}_2^0. \tag{A1}$$

Decay chain $(\mathrm{III})_1$ is relevant to the tb events. On the other hand, as decay chain $(\mathrm{I})_2$ has no W, sideband subtraction should remove events arising from the decay chain completely, unless there are accidental weak bosons or an underestimation of the misreconstructed events that has just been discussed above.

The branching ratio $\mathrm{Br}(\tilde{\chi}_2^0\to Z^0\tilde{\chi}_1^0)$ is small (1.5%) at point A1. The decay branching ratios at point A1 are

$$\mathrm{Br}(\mathrm{III})_1=\mathrm{Br}(\tilde{g}\to t\tilde{t}_1)\mathrm{Br}(\tilde{t}_1\to b\tilde{\chi}_1^{\pm})\times 0.7$$
$$=0.078,$$
$$\mathrm{Br}(\mathrm{I})_2=\mathrm{Br}(\tilde{g}\to b\tilde{b}_1)\mathrm{Br}(\tilde{b}_1\to b\tilde{\chi}_2^0)$$
$$=0.025, \tag{A2}$$

where the factor of 0.7 is the hadronic branching ratio of the W boson.

The numbers of reconstructed tb events before and after sideband subtraction are listed in Table X. For the K_T algorithm with $R=0.5$, the ratio of the numbers $N(\mathrm{I})_2/N(\mathrm{III})_1$ is 0.229 and 0.15 before and after sideband subtraction, respectively. Comparing these ratios to that of the branching ratios $\mathrm{Br}(\mathrm{I})_2/\mathrm{Br}(\mathrm{III})_1=0.32$, we see that the requirement $|m_{bjj}-m_t|<30$ GeV reduces the contribution of $(\mathrm{I})_2$ to about 70% relative to $(\mathrm{III})_1$ and it is further reduced to less than 50% after sideband subtraction. This ratio may be improved further by cutting events with $m_{jj}<70$ GeV or by using a more sophisticated background estimation.

[1] See references in H.P. Nilles, Phys. Rep. **110**, 1 (1984).

[2] ATLAS: Detector and physics performance technical design report No. CERN-LHCC-99-14.

[3] R. Barbieri, G.R. Dvali, and L.J. Hall, Phys. Lett. B **377**, 76 (1996).

[4] M. Dine, A. Kagan, and S. Samuel, Phys. Lett. B **243**, 250 (1990); S. Dimopoulos and G.F. Giudice, *ibid.* **357**, 573 (1995); A. Pomarol and D. Tommasini, Nucl. Phys. **B466**, 3 (1996); A.G. Cohen, D.B. Kaplan, and A.E. Nelson, Phys. Lett. B **388**, 588 (1996); J. Hisano, K. Kurosawa, and Y. Nomura, *ibid.* **445**, 316 (1999); Nucl. Phys. **B584**, 3 (2000).

[5] A.E. Nelson and M.J. Strassler, J. High Energy Phys. **09**, 030 (2000); T. Kobayashi and H. Terao, Phys. Rev. D **64**, 075003 (2001); T. Kobayashi, H. Nakano, and H. Terao, *ibid.* **65**, 015006 (2002); T. Kobayashi, H. Nakano, T. Noguchi, and H. Terao, *ibid.* **66**, 095011 (2002); J. High Energy Phys. **02**, 022 (2003).

[6] M. Carena and C.E. Wagner, Nucl. Phys. **B452**, 45 (1995).

[7] H.E. Haber and R. Hempfling, Phys. Rev. Lett. **66**, 1815 (1991); Y. Okada, M. Yamaguchi, and T. Yanagida, Prog. Theor. Phys. **85**, 1 (1991); J.R. Ellis, G. Ridolfi, and F. Zwirner, Phys. Lett. B **257**, 83 (1991); R. Barbieri and M. Frigeni, *ibid.* **258**, 395 (1991).

[8] R. Barbieri and G.F. Giudice, Phys. Lett. B **309**, 86 (1993).

[9] I. Hinchliffe, F.E. Paige, M.D. Shapiro, J. Soderqvist, and W. Yao, Phys. Rev. D **55**, 5520 (1997).

[10] J. Hisano, K. Kawagoe, R. Kitano, and M.M. Nojiri, Phys. Rev. D **66**, 115004 (2002).

[11] H. Baer, F.E. Paige, S.D. Protopopescu, and X. Tata, "ISAJET 7.48: a Monte Carlo event generator for pp, $\bar{p}p$, and e^+e^- reactions," hep-ph/0001086.

[12] T. Sjostrand, L. Lonnblad, and S. Mrenna, "PYTHIA 6.2: physics and manual," hep-ph/0108264.

[13] G. Corcella, I.G. Knowles, G. Marchesini, S. Moretti, K. Odagiri, P. Richardson, M.H. Seymour, and B.R. Webber, J. High Energy Phys. **01**, 010 (2001).

[14] E. Richter-Was *et al.*, ATLFAST 2.21, ATLAS Internal Note No. PHYS-NO-079.

[15] M. Battaglia *et al.*, Eur. Phys. J. C **22**, 535 (2001).

[16] J. Hisano, R. Kitano, and M.M. Nojiri, Phys. Rev. D **65**,

116002 (2002).

[17] D.R. Tovey, Phys. Lett. B **498**, 1 (2001); ATLAS NOTE ATL-PHYS-2002-013; EPJdirect C **4**, N4 (2002).

[18] B.C. Allanach *et al.*, in *Proceedings of the APS/DPF/DPB Summer Study on the Future of Particle Physics*, Snowmass, 2001, edited by N. Graf [Eur. Phys. J. C **25**, 113 (2002)].

[19] W.A. Bardeen, M. Carena, S. Pokorski, and C.E. Wagner, Phys. Lett. B **320**, 110 (1994).

[20] M. Bosman *et al.*, ''JET Finder Library: version 1.0,'' Report No. ATL-SOFT-98-038.